

# Coronal hole picoflare jets are the progenitors of both the fast and the Alfvénic slow solar wind

L. P. Chitta<sup>1</sup>, Z. Huang<sup>1</sup>, R. D’Amicis<sup>2</sup>, D. Calchetti<sup>1</sup>, A. N. Zhukov<sup>3,4</sup>, E. Kraaikamp<sup>3</sup>, C. Verbeeck<sup>3</sup>, R. Aznar Cuadrado<sup>1</sup>, J. Hirzberger<sup>1</sup>, D. Berghmans<sup>3</sup>, T. S. Horbury<sup>5</sup>, S. K. Solanki<sup>1</sup>, C. J. Owen<sup>6</sup>, L. Harra<sup>7,8</sup>, H. Peter<sup>1,9</sup>, U. Schühle<sup>1</sup>, L. Teriaca<sup>1</sup>, P. Louarn<sup>10</sup>, S. Livi<sup>11</sup>, A. S. Giunta<sup>12</sup>, D. M. Hassler<sup>13</sup>, Y.-M. Wang<sup>14</sup>

<sup>1</sup> Max-Planck-Institut für Sonnensystemforschung, 37077 Göttingen, Germany  
e-mail: chitta@mps.mpg.de

<sup>2</sup> National Institute for Astrophysics (INAF), Institute for Space Astrophysics and Planetology (IAPS), Via Fosso del Cavaliere, 100, 00133 Rome, Italy

<sup>3</sup> Solar-Terrestrial Centre of Excellence, Solar Influences Data analysis Centre, Royal Observatory of Belgium, 1180 Brussels, Belgium

<sup>4</sup> Skobel’syn Institute of Nuclear Physics, Moscow State University, 119991 Moscow, Russia

<sup>5</sup> Department of Physics, Imperial College London, SW7 2AZ London, UK

<sup>6</sup> Mullard Space Science Laboratory, Holmbury St Mary, RH5 6NT, UK

<sup>7</sup> Physikalisch-Meteorologisches Observatorium Davos, World Radiation Center, 7260 Davos Dorf, Switzerland

<sup>8</sup> Die Eidgenössische Technische Hochschule Zürich, 8093 Zürich, Switzerland

<sup>9</sup> Institut für Sonnenphysik (KIS), Georges-Köhler-Allee 401a, 79110 Freiburg, Germany

<sup>10</sup> Institut de Recherche en Astrophysique et Planétologie, CNRS, Université de Toulouse, CNES, Toulouse, France

<sup>11</sup> Southwest Research Institute, San Antonio, TX 78238, USA

<sup>12</sup> RAL Space, UKRI STFC Rutherford Appleton Laboratory, Didcot OX11 0QX, UK

<sup>13</sup> Southwest Research Institute, Boulder, CO 80302, USA

<sup>14</sup> Space Science Division, Naval Research Laboratory, Washington, DC 20375, USA

Received ; accepted

## ABSTRACT

The solar wind, classified by its bulk speed and the Alfvénic nature of its fluctuations, generates the heliosphere. The elusive physical processes responsible for the generation of the different types of the wind are a topic of active debate. Recent observations revealed intermittent jets with kinetic energy in the picoflare range, emerging from dark areas of a polar coronal hole threaded by open magnetic field lines. These could substantially contribute to the solar wind. However, their ubiquity and direct links to the solar wind have not been established. Here we report a unique set of remote-sensing and in-situ observations from the Solar Orbiter spacecraft, that establish a unified picture of the fast and Alfvénic slow wind, connected to the similar widespread picoflare jet activity in two coronal holes. Radial expansion of coronal holes ultimately regulates the speed of the emerging wind.

**Key words.** Sun: corona — Sun: magnetic fields — (Sun:) solar wind — Magnetic reconnection

## 1. Introduction

The heliosphere is a large-scale plasma bubble that extends to  $\sim 125$  astronomical units (au) from the Sun. It is generated by supersonic plasma outflows originating from the solar atmosphere. This solar wind (Parker 1958) has been traditionally characterized by its speed as measured near Earth. However, the growing consensus is that the Alfvénic nature of solar wind fluctuations is as crucial as the speed to fully comprehend the source regions of the wind (D’Amicis et al. 2021b; Wang 2024). This Alfvénicity is a high-degree of correlation between fluctuations of magnetic field and velocity components, accompanied by weak compressibility. This effect is theorized to be a consequence of magneto-hydrodynamic (MHD) large-amplitude Alfvén waves propagating outward from the Sun along the direction of average magnetic field (Belcher et al. 1969; Belcher & Davis 1971).

Fast wind with speed  $>500 \text{ km s}^{-1}$  is generally highly Alfvénic and emerges from the interiors of large coronal holes (Woch et al. 1997; McComas et al. 2000). Potential candidates for its origin include MHD waves associated with solar spicules

(De Pontieu et al. 2007; McIntosh et al. 2011; Shimizu et al. 2022; Skirvin et al. 2024) and magnetic reconnection powered jets at the coronal base (Tian et al. 2014; Tripathi et al. 2021; Kumar et al. 2022; Raouafi et al. 2023; Chitta et al. 2023b), both operating on small scales of  $<1000 \text{ km}$ . A component of the slow wind with speed  $<500 \text{ km s}^{-1}$  that is also Alfvénic is apparently linked to smaller, over-expanding coronal holes (D’Amicis & Bruno 2015; Wang & Ko 2019; Bale et al. 2019; D’Amicis et al. 2021b), and may form when large-scale pseudostreamers are present (Panasenco et al. 2019, 2020). But its connection to specific small-scale features in the solar atmosphere remains unclear (D’Amicis et al. 2021b).

As mentioned above, there is a growing evidence that, at least, the fast solar wind could originate from small-scale activity in the corona. As such, there is a wide variety of small-scale activity in the corona, particularly linked to jets powered by magnetic reconnection. For instance, extreme ultraviolet (EUV) observations from the high-resolution imager of the Extreme Ultraviolet Imager (EUI/HRI<sub>EUV</sub>) instrument (Rochus

et al. 2020) on the Solar Orbiter spacecraft (Müller et al. 2020), have shown a variety of small-scale jet activity in the quiet-Sun regions. These include reconnection-driven microjets that exhibit Y-shaped morphology (Hou et al. 2021), mini-filament eruptions associated with compact EUV brightenings (Panesar et al. 2021), and jets that rapidly evolve on timescales as short as 20 s (Chitta et al. 2021). But the contribution of such quiet-Sun jets to the solar wind is still unknown. Within coronal holes themselves, bright ray-like plumes, harbor numerous outward propagating features or jetlets (Raouafi & Stenborg 2014), which are considered to be a major source of the solar wind (Kumar et al. 2022; Raouafi et al. 2023). But plumes occupy only some 10% of a coronal hole volume (Ahmad & Withbroe 1977), and although expanding superradially, tend to keep their identity to altitudes of at least 15 solar radii (DeForest et al. 1997). Then the question of how such discrete plume structures would sustain a nearly space-filling solar wind needs further exploration.

Inter-plume regions, the darkest areas within coronal holes, are commonly considered to be the least active portions of the corona. In such inter-plume regions of a polar coronal hole, EUV/HRI<sub>EUV</sub> observations recently revealed intermittent tenuous outflows, that are a few 100 km wide (Chitta et al. 2023b). They have speeds of  $\sim 100 \text{ km s}^{-1}$  with kinetic energy content in the range consistent with those of picoflares ( $10^{21}$ – $10^{24}$  erg), and exhibit Y-shaped morphology at their origin, suggestive of a magnetic reconnection driver. The kinetic energy flux of these jets is  $\geq 10^5 \text{ erg cm}^{-2} \text{ s}^{-1}$  (Chitta et al. 2023b). This is comparable to the estimates of energetics at the sources of the fast wind streams that are thought to be launched by magnetic reconnection at the coronal base, as inferred from independent in-situ observations (Bale et al. 2023). The existence of such small-scale tenuous jets points to an intermittent origin of the solar wind from the interiors of coronal holes. However, their existence and ubiquity in other coronal holes, connection to the surface magnetic field, and direct link, if any, to the different types of the solar wind have not been established. The aim of this study is to investigate the base-level activity of inter-plume regions that form the majority of the ambient coronal hole and its potential link to the solar wind.

## 2. Observations

We made use of Solar Orbiter remote-sensing and in-situ data in our study. The observations were a part of L\_SMALL\_MRES\_MCAD\_Connection-Mosaic, a Solar Orbiter Observing Plan (SOOP) (Zouganelis et al. 2020; Auchère et al. 2020). The main purpose of this SOOP is to probe the connectivity of different types of the solar wind to their source regions. We considered observations from this SOOP obtained at two instances, the first of these was in the time frame 13–16 October 2022 (56 hours), and the second between 15–17 April 2023 (51 hours), with 6 pointings for each run. Here we analyzed one pointing for each set, and in particular the first pointing for the first set and the sixth pointing for the second set. Three remote-sensing instruments participated in this SOOP, EUV, SO-PHI, and Spectral Imaging of the Coronal Environment (SPICE) (SPICE Consortium et al. 2020). As described below, we used only the EUV and SO-PHI data to investigate the picoflare jet features as the spatial resolution of the SPICE instrument is not adequate to probe such small-scale features. Further details of the Solar Orbiter observations and all the other remote-sensing data that we used in this study are provided in Appendix A.

## 3. Origin of the fast wind streams

During its second science perihelion in October 2022, the Solar Orbiter spacecraft observed continuous streams of fast solar wind for about 7 days. In Fig. 1A–B we show the solar wind radial velocity and proton temperature over a 30 hour interval within this period, starting at 2022 October 14 00:00 Universal Time (UT), as measured by the Proton and Alpha Particle Sensor of the Solar Wind Analyzer (SWA-PAS) (Owen et al. 2020) onboard Solar Orbiter. These two parameters are generally positively correlated (Fig. A.1), a property which is interpreted to arise from the heating and acceleration of the solar wind close to the Sun (Démoulin 2009).

The radial component of the magnetic field in the solar wind measured by the Solar Orbiter magnetometer (MAG) (Horbury et al. 2020) has a predominantly negative polarity during this period (Fig. 1C), with frequent reversals in its orientation, referred to as switchbacks (Bale et al. 2019; Kasper et al. 2019) (Fig. A.2). We characterized the wind by evaluating its Alfvénicity,  $C_{VB}$ , measured by the correlation between the solar wind velocity and magnetic field (in Alfvén units) components, on timescales of 30 minutes (Appendix B). The fast wind is highly Alfvénic,  $C_{VB} \sim 1$ , throughout the period (Fig. 1D).

Consistent with in-situ magnetic field measurements, we found that the spacecraft is magnetically connected to a large coronal hole, threaded by magnetic field with dominant negative polarity, located in the southern hemisphere of the Sun (Figs. 1E–F, A.4, A.5). The spacecraft connectivity is persistent, within  $5^\circ$  in longitude, near the northern portion of that coronal hole over the course of a 24 hour interval within the considered 30 hour period. Considering the errors in back-tracing the solar wind plasma to the source surface (Appendix C), this persistence is strongly suggestive of the surrounding area within  $\sim 10^\circ$ – $16^\circ$  longitudinal separation being the source regions of the observed fast wind streams.

Accounting for the solar wind travel time, this 24 hour interval encompasses a high-resolution remote-sensing observing campaign of Solar Orbiter, which allows us to investigate the solar atmospheric dynamics at the base of the fast wind streams in an unprecedented way. The cluster of magnetic footpoints of the fast wind streams are all located directly adjacent to an inter-plume region in that coronal hole, that is conspicuous in the HRI<sub>EUV</sub> data (Fig. A.4). The underlying magnetic field is structured into network lanes, of predominantly negative polarity, as captured by the High Resolution Telescope, part of the Polarimetric and Helioseismic Imager instrument on the Solar Orbiter spacecraft (SO/PHI-HRT) (Solanki et al. 2020) (Fig. A.5). The flux imbalance in this case, measured as the absolute of the ratio of signed to the unsigned magnetic flux is about 0.8. We now use these high-resolution images and investigate the inter-plume region dynamics in order to further assess the level of background activity in this coronal hole.

In Fig. 2A we zoom into the coronal hole section with the inter-plume region and the underlying magnetic field. The dominant negative polarity magnetic field distribution is evident. We detected only a couple of closed-loop systems in this region. Most of the EUV emission is rather structured into a widespread jet activity, emerging from the underlying magnetic network, all propagating in the same direction (Movie S1). Slits S1–S7 mark some of the locations in the fainter areas of the inter-plume region where the jet activity is prolific. The space-time maps from these slits are displayed in Fig. 2B–H, which show slanted intensity ridges that indicate the propagation of the jets. Based on the intensity fluctuations we assess their lifetimes to be 60 s or

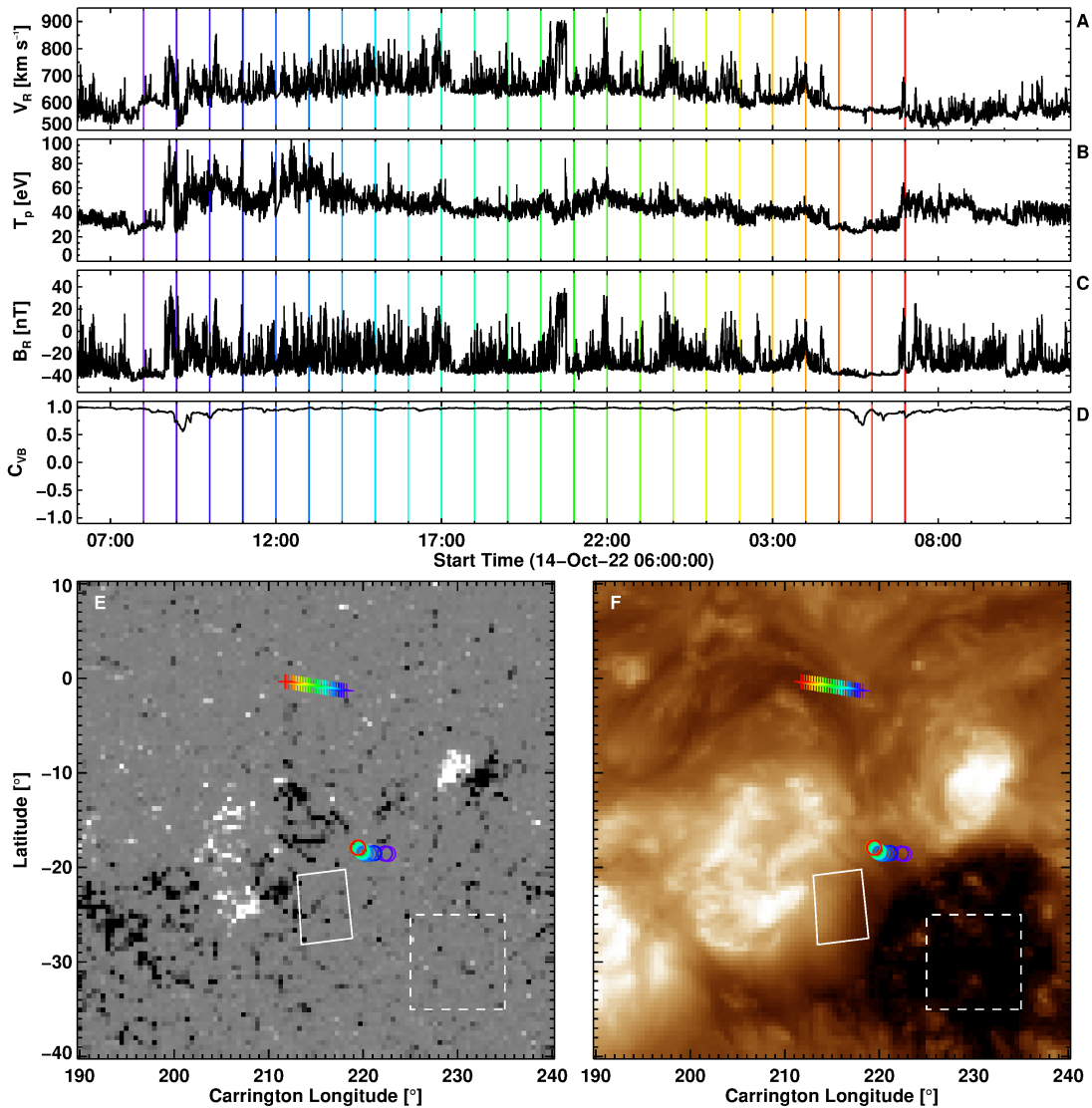


**Fig. 1.** Footpoint regions of the fast solar wind streams. (A) to (C) Time series of in-situ measurements of the solar wind radial velocity ( $V_R$ ), proton temperature ( $T_p$ ), and the radial component of the magnetic field in the solar wind ( $B_R$ ). (D) Alfvénicity of the solar wind ( $C_{VB}$ ). The vertical colored lines mark the time-stamps at 1 hour cadence over the course of a 24 hour period. Partial field of view (FOV) from the Carrington synoptic map (Carrington rotation number CR2263), showing the distribution of photospheric radial magnetic field with Helioseismic and Magnetic Imager (HMI) onboard the Solar Dynamics Observatory (SDO), saturated at  $\pm 100$  G (E), and coronal EUV emission with 193 Å filter on Atmospheric Imaging Assembly (AIA) of SDO (F). The sub-spacecraft points of Solar Orbiter on the Sun at 1 hour cadence, starting from 2022 October 14 UT 06:00, are indicated by colored plus symbols (colors correspond to the vertical lines in panels A–D). The respective colored circles represent locations of magnetic connectivity of the spacecraft onto the solar surface, based on a PFSS model. The solid rectangle outlines the partial FOV of the HRI<sub>EUV</sub> instrument shown in Figs. 2A and A.4A. The dashed square region is used to calculate the coronal hole expansion factor plotted in Fig. 5. See Appendices A, B, and C for details.

less. The repetitive nature of these faint jets is also evident in the space-time maps. The propagation speeds are in the range  $100 \text{ km s}^{-1}$  in the plane-of-sky. All these properties of the observed jets are consistent with those of the picoflare jet activity identified in a polar coronal hole (Chitta et al. 2023b).

#### 4. Origin of the Alfvénic slow wind streams

During the third science perihelion of the Solar Orbiter mission in April 2023, SWA-PAS recorded slow wind streams with speeds well below  $500 \text{ km s}^{-1}$  (Fig. 3A). Proton temperature (Fig. 3B) correlates with the wind speed and basically follows the correlation relation that was found in the case of the fast

wind, but now extended to lower values in the parameter space (Fig. A.1). Along with the in-situ magnetic field measurements from MAG (Fig. 3C), we determined that the wind streams are highly Alfvénic,  $C_{VB} \sim -1$ , similar to the previous case, but with brief episodes of non-Alfvénicity (Fig. 3D).

We found in this case that the spacecraft is magnetically connected to a smaller coronal hole in the northern hemisphere, with the dominant polarity being positive, which is consistent with in-situ measurements (Figs. 3E–F, A.6, A.7). Over the course of a 24 hour period, the spacecraft is persistently connected, to within  $5^\circ$  in longitude, to the coronal hole region. Upon examining the HRI<sub>EUV</sub> images (Fig. A.6) and accounting for the travel time of the solar wind, we found the darker inter-plume areas

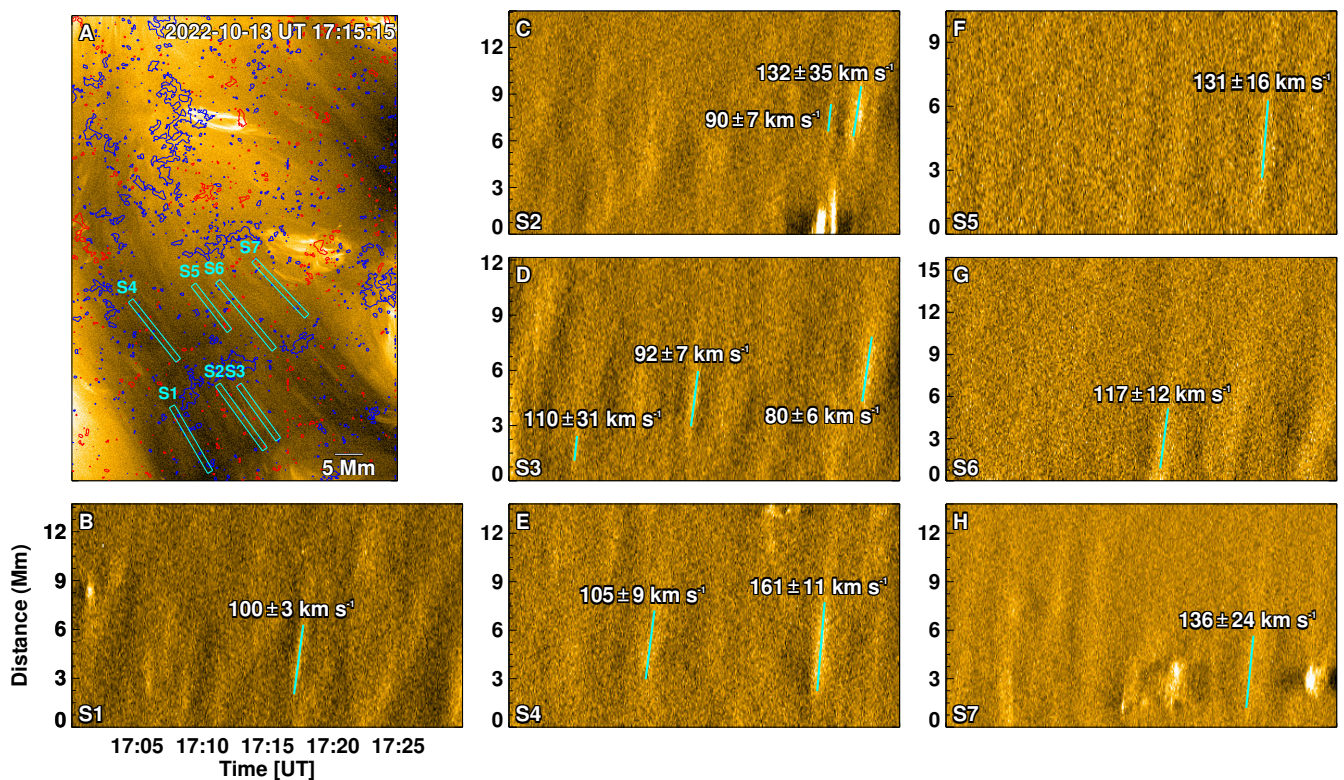


**Fig. 2.** Picoflare jets at the base of the fast wind. (A) Processed HRI<sub>EUV</sub> image of the coronal hole (FOV marked in Figs. 1E–F and A.4A). The contours outline photospheric magnetic field patches detected by SO/PHI-HRT (red: positive; blue: negative). An animated version of this panel is shown in Movie S1. Slanted rectangles S1–S7 are slits used to derive corresponding time-distance maps shown in panels B to H. In the time-distance maps (panels B to H), some of the jets are identified by slanted lines, the slopes of which denote the jet speeds as quoted. See Sect. 3 for details.

of the coronal hole adjacent to these connectivity footpoints. The underlying magnetic network of the positive polarity dominant field distribution, with a flux imbalance of about 0.4, is captured by the SO/PHI-HRT instrument (Fig. A.7). In this case, too, the inter-plume region is further structured into narrow jet features continuously emerging from the network lanes (Movie S2). Their properties (Fig. 4) are consistent with those seen near the footpoints of the fast wind streams.

## 5. Coronal hole expansion and the solar wind speed

Synoptic magnetic field maps used to trace the spacecraft connectivity (Figs. 1 and 3) were acquired at times that are different from the HRI<sub>EUV</sub> observations (Figs. 2 and 4). The structure of the coronal holes and the underlying magnetic field network distribution will have changed during this period. Nevertheless, the coronal holes and the inter-plume regions that we investigated here can be considered rather representative open magnetic field regions on the Sun from where the solar wind is expected to originate. Therefore, irrespective of having the precise knowledge of the spacecraft connectivity, our observations provide a solid picture that the same type of widespread small-scale jet activity is underlying the different types of the solar wind, both closely linked to the interiors of coronal holes (see Appendix C for discussion on uncertainties in the connectivity to a given source region).

It is now imperative to probe how the two coronal holes exhibiting seemingly similar picoflare jet activity sustain wind

streams with distinct speeds. It is empirically known that wind speeds are inversely proportional to how rapidly the magnetic field of coronal holes radially expands with height (Hundhausen 1972; Wang & Sheeley 1990). To this end, we measured this expansion factor for the two coronal holes under investigation (Appendix D). The corresponding distributions for the cases of the fast and the Alfvénic slow wind streams are displayed in Fig. 5. To support these calculations, we have also visually validated the degree of expansion of the coronal magnetic field at these locations based on the potential field source surface (PFSS) model with the observed coronal off-limb features (Figs. D.1 and D.2).

The expansion factor associated with the large coronal hole sustaining fast wind peaks at lower values compared to that of the smaller coronal hole sustaining slow wind. This is consistent with the scenario that larger flux-tube expansion leads to a steep fall-off in the energy dissipation with radial distance from the Sun, with most of it being dissipated inside the sonic point, causing an overall reduction in the wind speed (Wang 2020). A direct consequence of this could be seen in the overall reduction in the magnetic field fluctuations in the Alfvénic slow wind streams compared to those in the fast streams (Fig. A.2).

## 6. Discussion and Conclusion

Low spatial resolution spectroscopic observations provided signatures of persistent blueshifts of emission spectral lines in the transition region at the coronal base (indicative of upflows), over the boundaries of convective supergranules. Such spectral

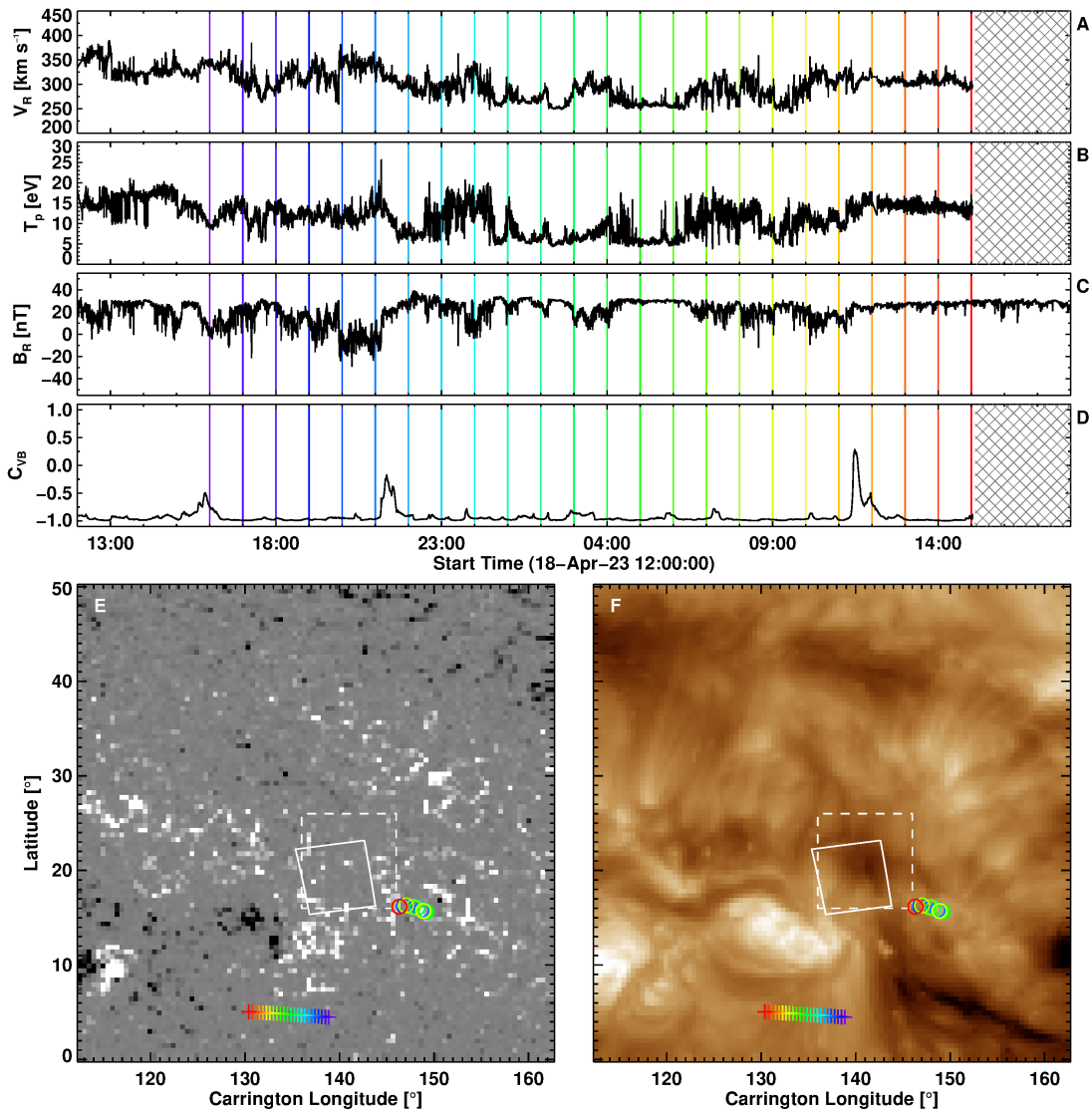


**Fig. 3.** Footpoint regions of the Alfvénic slow wind streams. Same as Fig. 1, but for observations of the Alfvénic slow wind streams in April 2023. Partial FOV of the synoptic maps in panels E and F correspond to CR2269. The hatched portion in panels A, B, and D indicate SWA-PAS data gaps.

blueshifts are hypothesized to be the signatures of the solar wind outflow at the coronal base (Hassler et al. 1999; Tu et al. 2005). However, it has also been demonstrated that blueshifts from coronal hole regions, that might otherwise be considered signatures of the fast wind, were substantially contaminated by the outflows from the ambient quiet Sun regions (Tian et al. 2011). But by employing SO/PHI-HRI and HRI<sub>EUV</sub> observations, acquired at nearly the same high spatial resolution, we are now able to trace individual faint jet features to the narrow magnetic network lanes in the interiors of coronal holes. Granular-scale emerging bipoles in the solar photosphere (Moore et al. 2011) facilitate continuous interactions between the parasitic polarity magnetic field patches and the network magnetic field (Gošić et al. 2014; Wang et al. 2022; Chitta et al. 2023a), leading to magnetic reconnection (Tu et al. 2005; Yang et al. 2013; Panesar et al. 2019; Pontin et al. 2024), and the launching of these picoflare jets from network lanes.

These tenuous jets form the most common and widespread background activity within the darker interiors of coronal holes. Their existence thus signifies the operation of magnetic recon-

nection at the base of the solar wind (Tu et al. 2005). The intermittency of the jets highlights the fleeting nature of the magnetic reconnection. While the observed picoflare jets at the coronal base themselves have not yet evolved into a fully-developed supersonic solar wind, they do propagate along the direction of the large-scale open magnetic field of coronal holes. Based on this we suggest that they are the dominant progenitors of the solar wind flow from those open field regions. In this scenario, as these jets reach higher altitudes and begin to merge, their transition to the solar wind outflow will be regulated by the degree of coronal hole expansion. Consequently, different types of the solar wind arise, as revealed by our MAG and SWA in-situ observations. In the case of October 2022 coronal hole, there are plume structures embedded within the EUV/HRI<sub>EUV</sub> field of view. As discussed in the Introduction, in line with earlier studies, these plumes also exhibit outward propagating disturbances or jet-like features. Characterization of these plume jets is an ongoing investigation.

Kink magnetohydrodynamic (MHD) waves appear to be quite apparent in spicular structures (McIntosh et al. 2011) and

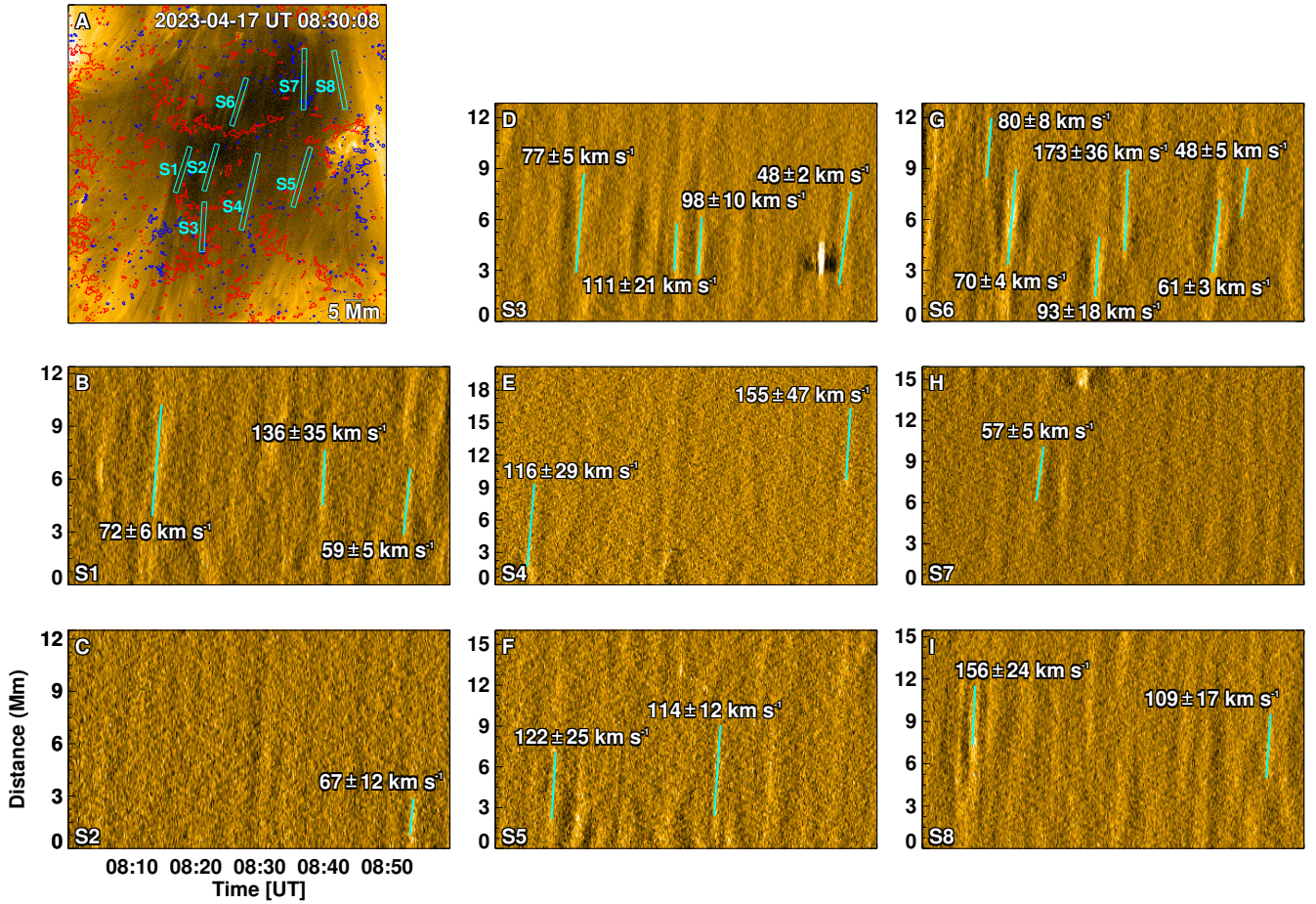


**Fig. 4.** Picroflare jets at the base of the Alfvénic slow wind streams. Same as Fig. 2 but for coronal hole observations on 2023 April 17. An animated version of panel A is shown in Movie S2.

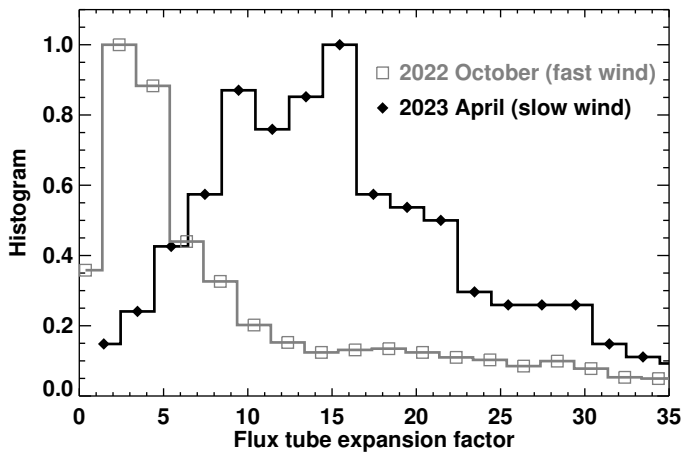


**Fig. 5.** Coronal hole expansion. Distribution of the expansion factors of magnetic field lines, at the source surface (2.5 solar radii), traced from the coronal hole sections identified with dashed boxes in Figs. 1E and 3E. The gray curve is for the case of the fast wind, while the black curve is for the case of the Alfvénic slow wind. See Appendices C and D for details.

transition region network jets (Tian et al. 2014). But we did not find obvious signatures of such kink waves in the HRI<sub>EUV</sub> ob-

servations of picroflare jets. If present, they must then exist on smaller spatial scales than the resolution limit of  $\sim 200$  km of the HRI<sub>EUV</sub> detector. In addition to kink waves, spicules also display persistent torsional Alfvén waves (De Pontieu et al. 2012; Srivastava et al. 2017). These waves are primarily detected as spicules showing alternating red- and blue-shifts of the spectral lines across their length.

Upon closer inspection, we found that picroflare jets exhibit a subtle intensity deflection propagating perpendicularly or obliquely to their jet propagation axis. These effects are better seen in the running difference images and the corresponding space-time maps, which we display in Fig. 6 for a sample of four jets. Similar deflections in the jet magnetic field are seen in numerical simulations (Pariat et al. 2009; Wyper et al. 2017) and their intensity signatures are captured as rotating spires in larger scale jets (Panesar et al. 2022; Long et al. 2023). Based on the similarities, we interpret these deflections as manifestations of torsional Alfvénic waves generated during the magnetic reconnection that produced the jet in the first place.

Unlike spicular torsional Alfvén waves that exhibit (quasi-periodic) oscillatory behavior (De Pontieu et al. 2012; Srivastava et al. 2017), we found that the intensity deflections in picroflare jets are pulse-like, meaning that we do not see repetitiveness. Furthermore, the deflections are unidirectional, implying that the jets have fixed chirality as we do not observe back-and-forth oscillations of the deflections. For instance, the jet in

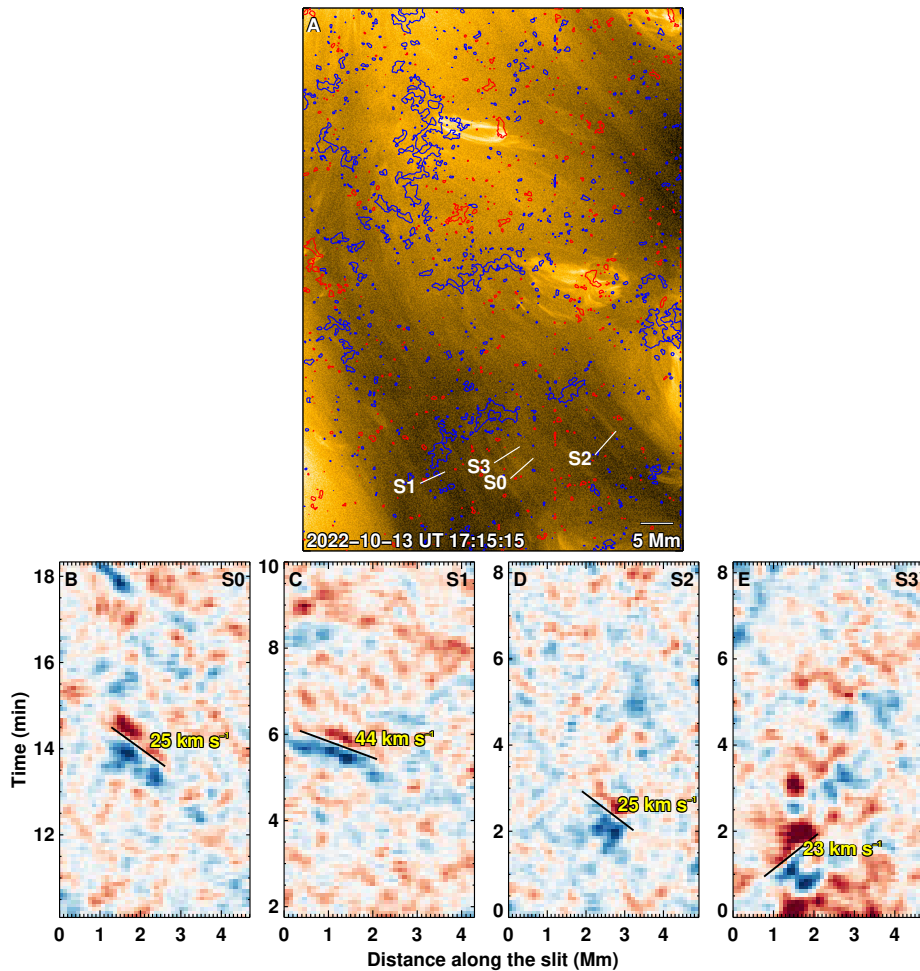


**Fig. 6.** Alfvénic pulses launched by picroflare jets. (A) Background image and contours are same as in Fig. 2A. Lines S0–S3 are slits placed perpendicular to the length of the jet. Panels (B) to (E) are running-difference space-time maps along the corresponding slits from panel (A). Red to blue color transition represents the intensity propagation perpendicular to the picroflare jet axis. The slanted black lines are overlaid on these propagating features to guide the eye. Their slopes in the units of speed ( $\text{km s}^{-1}$ ) are also quoted. Zero along the spatial axis represents the left edge of the slit, while the origin of the time axis is with respect to the start time of the observations. An animated version of the Alfvénic pulse in panel B is shown in Movie S3.

Fig. 6E has a sense of chirality that is opposite to the jets in Fig. 6B–D. The deflection speeds are comparable to the average tangential flow of the solar wind (Fig. A.3). Despite their pulse-like behavior, deflection speeds are consistent with velocity amplitudes of chromospheric torsional motions (De Pontieu et al. 2012). Such perturbations could be produced by the eruption of a highly sheared bundle of the magnetic field (Sterling & Moore 2020) or launched by magnetic reconnection outflows coupled to photospheric vortex flows (Asensio Ramos et al. 2017). These torsional perturbations propagate with speeds over  $20 \text{ km s}^{-1}$  (Fig. 6, Movie S3). The speeds are comparable to the average values of the solar wind tangential velocity measured in-situ (Fig. A.3).

The observed small-scale dynamics of the jets thus have direct implications for the large-scale properties of the solar wind, that are not yet fully understood. On the one hand the torsional Alfvénic pulses detected in our high-resolution coronal images would generate perturbations that will grow to produce the rotational flows in the solar wind (Kasper et al. 2019). On the other hand, the chirality of these Alfvénic pulses implies that the underlying magnetic field perturbations are polarized already low in the corona, at the base of the solar wind. These polar-

ized magnetic field perturbations coupled with the Parker spiral (non-radial component of the mean magnetic field in the solar wind) and dragged outward by the expanding solar wind (Johnston et al. 2022; Squire et al. 2022) might explain the asymmetries in the switchbacks patches in the (inner) heliosphere (Bale et al. 2021). Our analysis using the unprecedented combination of the high-resolution remote-sensing and in-situ measurements from the inner heliosphere presented here thus provides the most comprehensive picture yet of the direct role of small-scale jets originating from interiors of coronal holes in seeding the solar wind outflow with its characteristic large-scale properties.

*Acknowledgements.* We thank the anonymous referee for many constructive comments that helped us improve the presentation of the manuscript. This project has received funding from the European Research Council (ERC) under the European Union’s Horizon 2020 research and innovation programme (grant agreement Nos. 10103984 – project ORIGIN; 101097844 – project WINSUN). ZH conducted the work in this paper in the framework of the International Max Planck Research School (IMPRS) for Solar System Science at the Technical University of Braunschweig. ANZ, EK, CV, and DB thank the Belgian Federal Science Policy Office (BELSPO) for the provision of financial support in the framework of the PRODEX Programme of the European Space Agency (ESA) under contract numbers 4000136424 and 4000143743. This work was supported by NASA and the Office of Naval Research. Solar Orbiter is a space mission of international collaboration between ESA and NASA, operated by ESA. We

thank the ESA SOC and MOC teams for their support. The EUI instrument was built by CSL, IAS, MPS, MSSL/UCL, PMOD/WRC, ROB, LCF/IO with funding from the Belgian Federal Science Policy Office (BELSPO/PRODEX PEA 4000106864 and 4000112292); the Centre National d'Etudes Spatiales (CNES); the UK Space Agency (UKSA); the Bundesministerium für Wirtschaft und Energie (BMWi) through the Deutsches Zentrum für Luft- und Raumfahrt (DLR); and the Swiss Space Office (SSO). The Solar Orbiter magnetometer was funded by the UKSA (grant ST/T001062/1). The German contribution to SO/PHI is funded by the BMWi through DLR and by MPG central funds. The Spanish contribution is funded by AEI/MCIN/10.13039/501100011033/ and European Union "NextGenerationEU"/PRTR" (RTI2018-096886-C5, PID2021-125325OB-C5, PCI2022-135009-2, PCI2022-135029-2) and ERDF "A way of making Europe"; "Center of Excellence Severo Ochoa" awards to IAA-CSIC (SEV-2017-0709, CEX2021-001131-S); and a Ramón y Cajal fellowship awarded to DOS. The French contribution is funded by CNES. The Solar Orbiter Solar Wind Analyser (SWA) data are derived from scientific sensors that have been designed and created, and are operated under funding provided in numerous contracts from the UKSA, the UK Science and Technology Facilities Council (STFC), the Agenzia Spaziale Italiana (ASI), CNES, France, the Centre National de la Recherche Scientifique (CNRS, France), the Czech contribution to the ESA PRODEX programme, and NASA. Solar Orbiter SWA work at UCL/MSSL is funded under STFC grants ST/X002152/1, and ST/W001004/1. SDO is the first mission to be launched for NASA's Living With a Star (LWS) Program and the data supplied courtesy of the HMI and AIA consortia. We thank the GOES team for making the data publicly available. This research has made use of NASA's Astrophysics Data System Bibliographic Services. SDO/AIA synoptic maps (Illarionov et al. 2020) are available at [https://sun.njit.edu/#/coronal\\_holes](https://sun.njit.edu/#/coronal_holes). SUVI data are available via the NCEI/GOES-R Space Weather data website: <https://www.ngdc.noaa.gov/stp/satellite/goes-r.html>. AIAPY open source software package v0.7.3 (Barnes et al. 2020, 2021), SSWIDL (Freeland & Handy 1998), PFSS module (Schrijver & De Rosa 2003) are used for data analysis.

## References

- Ahmad, I. A. & Withbroe, G. L. 1977, *Sol. Phys.*, 53, 397
- Asensio Ramos, A., Requerey, I. S., & Vitas, N. 2017, *A&A*, 604, A11
- Auchère, F., Andretta, V., Antonucci, E., et al. 2020, *A&A*, 642, A6
- Bale, S. D., Badman, S. T., Bonnell, J. W., et al. 2019, *Nature*, 576, 237
- Bale, S. D., Drake, J. F., McManus, M. D., et al. 2023, *Nature*, 618, 252
- Bale, S. D., Horbury, T. S., Velli, M., et al. 2021, *ApJ*, 923, 174
- Barnes, W., Cheung, M., Bobra, M., et al. 2021, *ATAPY*, Zenodo. 10.5281/zenodo.5606094
- Barnes, W. T., Cheung, M. C. M., Bobra, M. G., et al. 2020, *Journal of Open Source Software*, 5, 2801
- Belcher, J. W. & Davis, Leverett, J. 1971, *J. Geophys. Res.*, 76, 3534
- Belcher, J. W., Davis, Leverett, J., & Smith, E. J. 1969, *J. Geophys. Res.*, 74, 2302
- Boerner, P., Edwards, C., Lemen, J., et al. 2012, *Sol. Phys.*, 275, 41
- Bruno, R., Carbone, V., Primavera, L., et al. 2004, *Annales Geophysicae*, 22, 3751
- Cheng, X., Priest, E. R., Li, H. T., et al. 2023, *Nature Communications*, 14, 2107
- Chitta, L. P., Peter, H., Parenti, S., et al. 2022, *A&A*, 667, A166
- Chitta, L. P., Solanki, S. K., del Toro Iniesta, J. C., et al. 2023a, *ApJ*, 956, L1
- Chitta, L. P., Solanki, S. K., Peter, H., et al. 2021, *A&A*, 656, L13
- Chitta, L. P., Zhukov, A. N., Berghmans, D., et al. 2023b, *Science*, 381, 867
- Dakeyo, J. B., Badman, S. T., Rouillard, A. P., et al. 2024, *A&A*, 686, A12
- D'Amicis, R. & Bruno, R. 2015, *ApJ*, 805, 84
- D'Amicis, R., Bruno, R., Panasenco, O., et al. 2021a, *A&A*, 656, A21
- D'Amicis, R., Perrone, D., Bruno, R., & Velli, M. 2021b, *Journal of Geophysical Research (Space Physics)*, 126, e28996
- Darnel, J. M., Seaton, D. B., Bethge, C., et al. 2022, *Space Weather*, 20, e2022SW003044
- De Pontieu, B., Carlsson, M., Rouppe van der Voort, L. H. M., et al. 2012, *ApJ*, 752, L12
- De Pontieu, B., McIntosh, S. W., Carlsson, M., et al. 2007, *Science*, 318, 1574
- DeForest, C. E., Hoeksema, J. T., Gurman, J. B., et al. 1997, *Sol. Phys.*, 175, 393
- Démoulin, P. 2009, *Sol. Phys.*, 257, 169
- Freeland, S. L. & Handy, B. N. 1998, *Sol. Phys.*, 182, 497
- Gissot, S., Auchère, F., Berghmans, D., et al. 2023, *arXiv e-prints*, [arXiv:2307.14182](https://arxiv.org/abs/2307.14182)
- Gošić, M., Bellot Rubio, L. R., Orozco Suárez, D., Katsukawa, Y., & del Toro Iniesta, J. C. 2014, *ApJ*, 797, 49
- Hassler, D. M., Dammach, I. E., Lemaire, P., et al. 1999, *Science*, 283, 810
- Horbury, T. S., O'Brien, H., Carrasco Blazquez, I., et al. 2020, *A&A*, 642, A9
- Hou, Z., Tian, H., Berghmans, D., et al. 2021, *ApJ*, 918, L20
- Hundhausen, A. J. 1972, *Coronal Expansion and Solar Wind* (Springer Berlin, Heidelberg)
- Illarionov, E., Kosovichev, A., & Tlatov, A. 2020, *ApJ*, 903, 115
- Johnston, Z., Squire, J., Mallet, A., & Meyrand, R. 2022, *Physics of Plasmas*, 29, 072902
- Kahil, F., Gandorfer, A., Hirzberger, J., et al. 2023, *A&A*, 675, A61
- Kahil, F., Gandorfer, A., Hirzberger, J., et al. 2022, in *Society of Photo-Optical Instrumentation Engineers (SPIE) Conference Series*, Vol. 12180, *Space Telescopes and Instrumentation 2022: Optical, Infrared, and Millimeter Wave*, ed. L. E. Coyle, S. Matsuura, & M. D. Perrin, 121803F
- Kasper, J. C., Bale, S. D., Belcher, J. W., et al. 2019, *Nature*, 576, 228
- Koukras, A., Dolla, L., & Keppens, R. 2022, in *SHINE 2022 Workshop*, 68
- Kraaikamp, E., Gissot, S., Stegen, K., et al. 2023, *Solo/EUI Data Release 6.0*, published by Royal Observatory of Belgium (ROB). 10.24414/z818-4163
- Kumar, P., Karpen, J. T., Uritsky, V. M., et al. 2022, *ApJ*, 933, 21
- Lemen, J. R., Title, A. M., Akin, D. J., et al. 2012, *Sol. Phys.*, 275, 17
- Long, D. M., Chitta, L. P., Baker, D., et al. 2023, *ApJ*, 944, 19
- Macneil, A. R., Owens, M. J., Finley, A. J., & Matt, S. P. 2022, *MNRAS*, 509, 2390
- Mandal, S., Chitta, L. P., Peter, H., et al. 2022, *A&A*, 664, A28
- Markwardt, C. B. 2009, in *Astronomical Society of the Pacific Conference Series*, Vol. 411, *Astronomical Data Analysis Software and Systems XVIII*, ed. D. A. Bohlender, D. Durand, & P. Dowler, 251
- McComas, D. J., Barraclough, B. L., Funsten, H. O., et al. 2000, *J. Geophys. Res.*, 105, 10419
- McIntosh, S. W., de Pontieu, B., Carlsson, M., et al. 2011, *Nature*, 475, 477
- Moore, R. L., Sterling, A. C., Cirtain, J. W., & Falconer, D. A. 2011, *ApJ*, 731, L18
- Morgan, H. & Druckmüller, M. 2014, *Sol. Phys.*, 289, 2945
- Müller, D., St. Cyr, O. C., Zouganelis, I., et al. 2020, *A&A*, 642, A1
- Nolte, J. T. & Roelof, E. C. 1973, *Sol. Phys.*, 33, 241
- Owen, C. J., Bruno, R., Livi, S., et al. 2020, *A&A*, 642, A16
- Panasenco, O., Velli, M., D'Amicis, R., et al. 2020, *ApJS*, 246, 54
- Panasenco, O., Velli, M., & Panasenco, A. 2019, *ApJ*, 873, 25
- Panesar, N. K., Sterling, A. C., Moore, R. L., et al. 2019, *ApJ*, 887, L8
- Panesar, N. K., Tiwari, S. K., Berghmans, D., et al. 2021, *ApJ*, 921, L20
- Panesar, N. K., Tiwari, S. K., Moore, R. L., Sterling, A. C., & De Pontieu, B. 2022, *ApJ*, 939, 25
- Pariat, E., Antiochos, S. K., & DeVore, C. R. 2009, *ApJ*, 691, 61
- Parker, E. N. 1958, *ApJ*, 128, 664
- Pesnell, W. D., Thompson, B. J., & Chamberlin, P. C. 2012, *Sol. Phys.*, 275, 3
- Poljančič Beljan, I., Jurdana-Šepić, R., Brajša, R., et al. 2017, *A&A*, 606, A72
- Pontin, D. I., Priest, E. R., Chitta, L. P., & Titov, V. S. 2024, *ApJ*, 960, 51
- Raouafi, N. E. & Stenborg, G. 2014, *ApJ*, 787, 118
- Raouafi, N. E., Stenborg, G., Seaton, D. B., et al. 2023, *ApJ*, 945, 28
- Rochus, P., Auchère, F., Berghmans, D., et al. 2020, *A&A*, 642, A8
- Schatten, K. H., Wilcox, J. M., & Ness, N. F. 1969, *Sol. Phys.*, 6, 442
- Scherrer, P. H., Schou, J., Bush, R. I., et al. 2012, *Sol. Phys.*, 275, 207
- Schrijver, C. J. & De Rosa, M. L. 2003, *Sol. Phys.*, 212, 165
- Seaton, D. B., Berghmans, D., Bloomfield, D. S., et al. 2023, *Sol. Phys.*, 298, 92
- Shimizu, K., Shoda, M., & Suzuki, T. K. 2022, *ApJ*, 931, 37
- Sinjan, J., Calchetti, D., Hirzberger, J., et al. 2022, in *Society of Photo-Optical Instrumentation Engineers (SPIE) Conference Series*, Vol. 12189, *Society of Photo-Optical Instrumentation Engineers (SPIE) Conference Series*, 121891J
- Skirvin, S. J., Samanta, T., & Van Doorselaere, T. 2024, *A&A*, 689, A135
- Solanki, S. K., del Toro Iniesta, J. C., Woch, J., et al. 2020, *A&A*, 642, A11
- SPIE Consortium, Anderson, M., Appourchaux, T., et al. 2020, *A&A*, 642, A14
- Squire, J., Johnston, Z., Mallet, A., & Meyrand, R. 2022, *Physics of Plasmas*, 29, 112903
- Srivastava, A. K., Shetye, J., Murawski, K., et al. 2017, *Scientific Reports*, 7, 43147
- Sterling, A. C. & Moore, R. L. 2020, *ApJ*, 896, L18
- Sun, X., Liu, Y., Hoeksema, J. T., Hayashi, K., & Zhao, X. 2011, *Sol. Phys.*, 270, 9
- Thompson, W. T. 2006, *A&A*, 449, 791
- Tian, H., DeLuca, E. E., Cranmer, S. R., et al. 2014, *Science*, 346, 1255711
- Tian, H., McIntosh, S. W., Habbal, S. R., & He, J. 2011, *ApJ*, 736, 130
- Tripathi, D., Nived, V. N., & Solanki, S. K. 2021, *ApJ*, 908, 28
- Tu, C. Y., Marsch, E., & Thieme, K. M. 1989, *J. Geophys. Res.*, 94, 11739
- Tu, C.-Y., Zhou, C., Marsch, E., et al. 2005, *Science*, 308, 519
- Wang, J., Lee, J., Liu, C., Cao, W., & Wang, H. 2022, *ApJ*, 924, 137
- Wang, Y. M. 2020, *ApJ*, 904, 199
- Wang, Y. M. 2024, *Sol. Phys.*, 299, 54
- Wang, Y. M. & Ko, Y. K. 2019, *ApJ*, 880, 146
- Wang, Y. M. & Sheeley, N. R., Jr. 1990, *ApJ*, 355, 726
- Woch, J., Axford, W. I., Mall, U., et al. 1997, *Geophys. Res. Lett.*, 24, 2885
- Wyper, P. F., Antiochos, S. K., & DeVore, C. R. 2017, *Nature*, 544, 452
- Yang, L., He, J., Peter, H., et al. 2013, *ApJ*, 770, 6
- Zouganelis, I., De Groof, A., Walsh, A. P., et al. 2020, *A&A*, 642, A3

## Appendix A: Observations and Data Processing

### A.1. Solar Orbiter in-situ data

For in-situ measurements of the solar wind plasma parameters including the velocity and proton temperature, we used data from Proton and Alpha Particle Sensor of the Solar Wind Analyzer (SWA-PAS) (Owen et al. 2020) on the Solar Orbiter spacecraft. In particular, we used level-2 data of type SOLO\_L2\_SWA-PAS-GRND-MOM, which have a cadence of 4 s. In-situ measurements of the magnetic field in the solar wind were retrieved by the Solar Orbiter magnetometer (MAG) (Horbury et al. 2020). We used level-2 MAG data of type SOLO\_L2\_MAG-RTN-NORMAL, with a cadence of 0.125 s.

Velocity and magnetic field components are in the heliographic Radial, Tangential, and Normal (RTN) coordinate system, where R points away from the Sun toward the spacecraft, T is the cross product of the solar spin axis and R (roughly along the orbital direction of the spacecraft), with N completing the right-handed system.

A scatter plot between the proton temperature and radial velocity is shown in Fig. A.1. These two quantities are generally well correlated as described in the main text. To characterize the in-situ magnetic field evolution, we zoomed into a shorter 1 hour interval as shown in Fig. A.2. Accounting for the solar wind travel time, the chosen time periods fall close to the respective remote-sensing observations. Compared to the Alfvénic slow wind streams, magnetic field in the fast wind streams exhibits larger variations and polarity reversals termed switchbacks (Fig. A.2A and C). To quantify magnetic field fluctuations in this period (Bruno et al. 2004; D’Amicis et al. 2021a), we also calculated the displacement of the magnetic field vector as a function of time,  $|\delta B(t)|$ , with respect to an arbitrary direction, fixed by the magnetic field vector at the start of the considered 1 hour time interval,  $B(t_0)$ , as

$$|\delta B(t)| = \sqrt{\sum_{i=R,T,N} (B_i(t) - B_i(t_0))^2}. \quad (\text{A.1})$$

The quantity is then normalized by the magnitude of the magnetic field vector,  $\langle B \rangle$ , and the results are plotted in Fig. A.2B and D. Magnetic field in the fast solar wind streams exhibits larger displacement compared to that of the Alfvénic slow wind streams.

Additionally, we used in-situ velocity measurements averaged over 1 hour timescales to trace the footpoints of magnetic fields and investigate the tangential solar wind flows (Fig. A.3) as described in the following sections. These data (SOLO\_COHO1HR\_MERGED\_MAG\_PLASMA) are archived at Coordinated Data Analysis Web.

### A.2. Solar Orbiter remote-sensing data

For the remote-sensing observations of coronal holes we used the extreme ultraviolet (EUV) image sequence in the 174 Å pass-band acquired by the HRI<sub>EUV</sub> instrument during the second and third science perihelion campaigns of the Solar Orbiter spacecraft. During the first of these observing campaigns on 2022 October 13 that was carried out between 17:00 and 17:30 Universal Time (UT), the spacecraft was at a distance of 0.293 astronomical units (au) from the Sun. The images were recorded at a cadence of 5 s, with an exposure time of 2.8 s, and have an image scale of 0.492 arcseconds (") pixel<sup>-1</sup>. The spatial resolution of HRI<sub>EUV</sub> during the period of these observations was

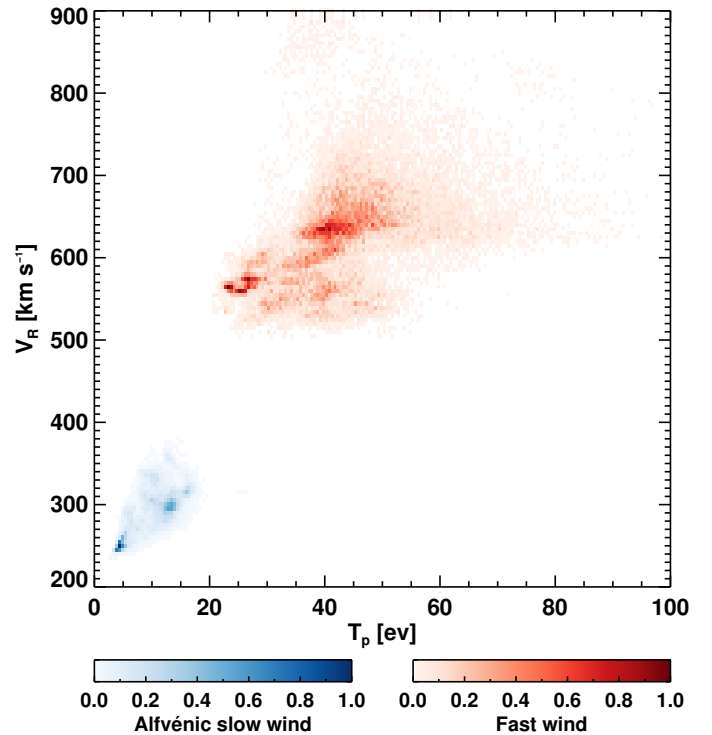


**Fig. A.1.** Proton temperature and radial velocity correlation. Two-dimensional histograms of  $T_p$  vs.  $V_R$ . The red population corresponds to the fast wind streams presented in Fig. 1, whereas the blue population corresponds to data from the Alfvénic slow wind streams from Fig. 3. The normalized population density is indicated by the respective color-bar.

about 209 km on the Sun (the full width at half maximum of the core of the point spread function of HRI<sub>EUV</sub> instrument is about two pixels). These data have a field of view (FOV) of  $\sim 214 \text{ Mm} \times 214 \text{ Mm}$ , sampled by  $2048 \times 2048$  pixels.

The second observing campaign data that we used were from 2023 April 17 between 08:00 UT and 09:00 UT, when the spacecraft was at a distance of 0.33 au. The EUV images were recorded at a cadence of 10 s, with an exposure time of 5 s, spatial resolution of 236 km, and FOV of  $\sim 241 \text{ Mm} \times 241 \text{ Mm}$ . We used level-2 data from this observing campaign (Kraaikamp et al. 2023). The jitter in the level-2 HRI<sub>EUV</sub> data was removed following the cross-correlation methodology described in Chitta et al. (2022, 2023b). For visualization purposes, we re-binned the HRI<sub>EUV</sub> data to an effective cadence of 30 s, by averaging an appropriate number of images from each campaign. Furthermore, we applied a multi-scale Gaussian normalization technique (Morgan & Druckmüller 2014) to enhance the contrast of the faint features in the dark regions of the coronal holes.

To provide extended coronal context to the HRI<sub>EUV</sub> observations, we used EUV 174 Å data from the Full Sun Imager (FSI) of the EUI instrument. For this purpose, we employed level-2 FSI images, one map from each of the two observing campaigns, recorded close to the start time of the above mentioned observational period. The context HRI<sub>EUV</sub> and FSI images from the two datasets are displayed in panels A and B of Figs. A.4 and A.6, respectively. The HRI<sub>EUV</sub> and FSI 174 Å filters have dominant contributions from emission lines of Fe IX (at 171.1 Å) and Fe X (at 174.5 Å and 177.2 Å) and their thermal response peak is around temperatures of about 1 MK.

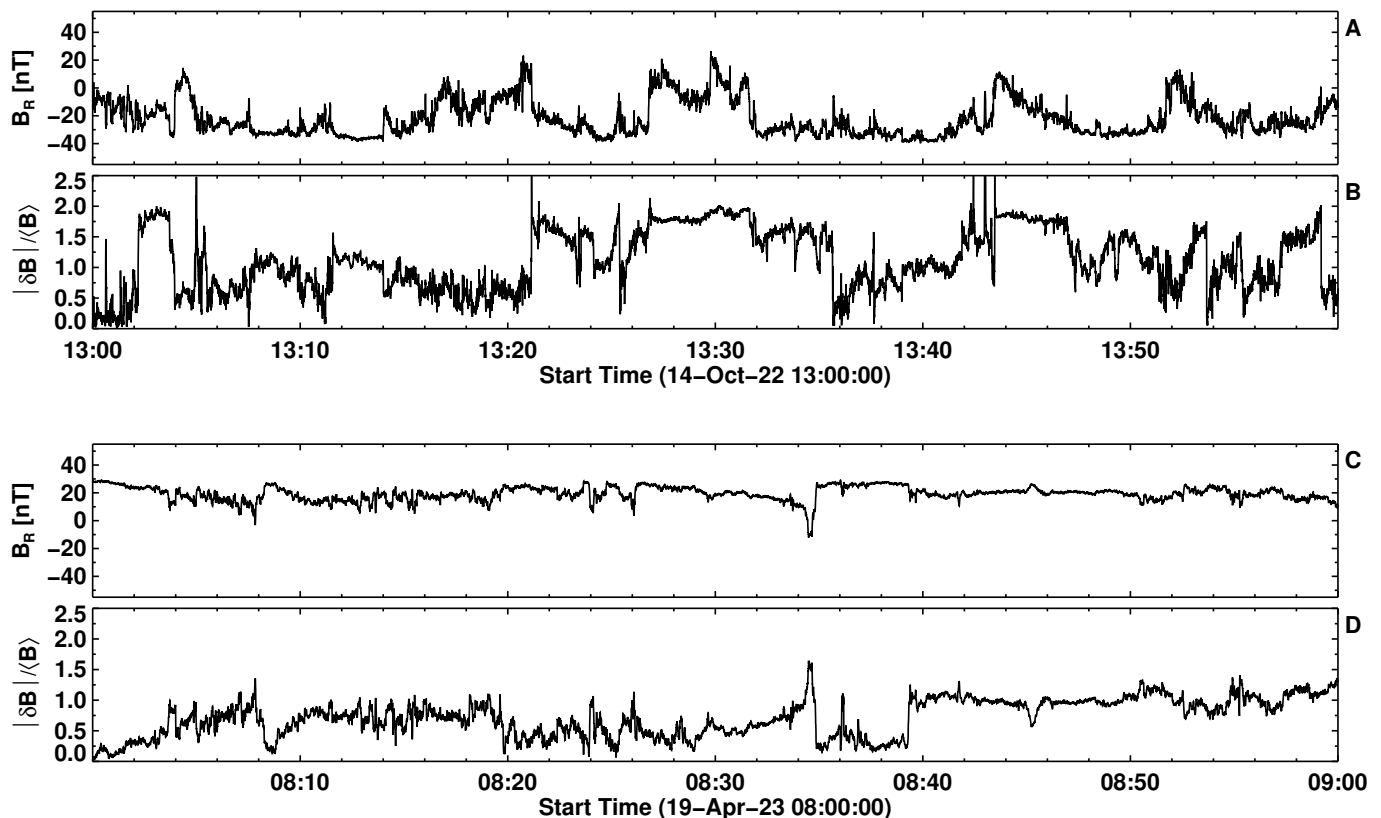


**Fig. A.2.** Magnetic field fluctuations in the solar wind. (A) Zoom into Fig. 1C, showing the time profile of the radial magnetic field in the fast wind streams over a 1 hour interval. (B) Fluctuations in the corresponding magnetic field vector normalized to its magnitude. (C) and (D) are the same as panels (A) and (B) but plotted for the case of the Alfvénic slow wind streams (Fig. 3C).

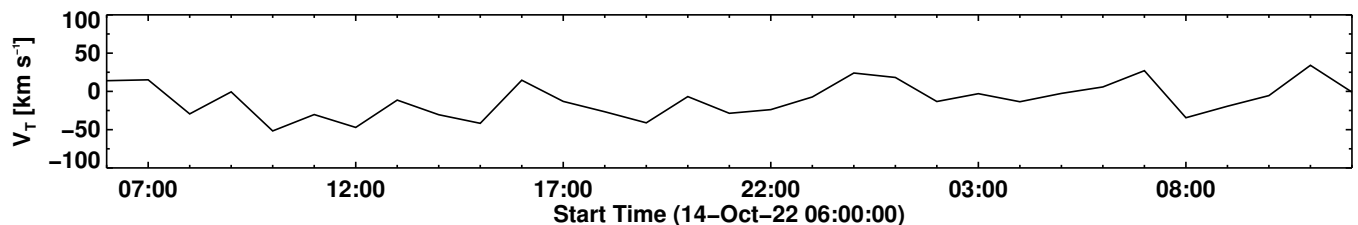


**Fig. A.3.** Tangential flows associated with the fast solar wind streams. Same as Fig. 1A but plotted for the in-situ time series of the 1 hour averaged tangential velocity ( $V_T$ ) of the fast solar wind during the October 2022 time frame.

We combined the coronal EUV data with photospheric line-of-sight magnetic field information obtained by the High Resolution Telescope of the Polarimetric and Helioseismic Imager instrument (SO/PHI-HRT) (Solanki et al. 2020). The SO/PHI-HRT instrument samples all four Stokes parameters at five wavelength positions in the Fe I 617.3 nm line plus a sixth one in the nearby continuum. Details of SO/PHI data reduction and calibration are available in Kahil et al. (2022); Sinjan et al. (2022); Kahil et al. (2023). SO/PHI-HRT data have an image scale of  $0.5'' \text{ pixel}^{-1}$ . During the first observing campaign, SO/PHI-HRT obtained a single magnetogram map on 2022 October 13 at 16:30 UT, i.e., 30 minutes prior to the EUV observations, with FOV of  $\sim 163 \text{ Mm} \times 163 \text{ Mm}$  (Fig. A.5A). Similarly, SO/PHI-HRT obtained a single magnetogram map on 2023 April 17 at 08:00 UT with FOV of  $\sim 245 \text{ Mm} \times 245 \text{ Mm}$ , during the second observing campaign (Fig. A.7A).

We re-scaled the SO/PHI-HRT maps to the pixel scale of HRI<sub>EUV</sub> and the photospheric magnetograms are visually co-aligned to the coronal EUV images with the aid of prominent surface bipolar magnetic patches and the overlying coronal loop systems. The two SO/PHI-HRT datasets and their FOV overlapping the HRI<sub>EUV</sub> images are shown in panel A of Figs. A.5 and A.7, respectively. Root-mean-square fluctuations of the magnetic field strength in the SO/PHI-HRT data have a standard deviation of about 10 G (2022 October) and 8.2 G (2023 April). We considered these values to be an upper limit on the corresponding noise level in the inferred line-of-sight component of the magnetic field. Contours plotted in Figs. 2A, 6A, and 4A outline magnetic patches with field strengths above  $3\times$  the upper limit on the noise level in the respective SO/PHI-HRT maps. The flux imbalance measures we quoted in the main text (about 0.8 in the case of 2022 October coronal hole, and 0.4 in the case of 2023 April coronal hole) based on the SO/PHI-HRT data are

computed by considering only those pixels where the magnetic field strength is at least  $3\times$  the noise upper limit.

### A.3. Solar Dynamics Observatory data

Earth Ecliptic longitudes of the first and second Solar Orbiter observing campaigns were  $-108^\circ$  (i.e., on the far side near east limb as seen from Earth), and  $107^\circ$  (on the far side near west limb as seen from Earth), respectively. These near-quadrate alignments mean that there were no observations from the Earth-bound space- and ground-based observatories at those times. But the coronal holes under investigation were long-living features and their evolution could be followed also from Earth view at times prior to and after the Solar Orbiter observing campaigns.

The first coronal hole observed close to the central meridian from the Solar Orbiter perspective around 2022 October 13 came into Earth view some 5 days later. Similarly, the second coronal hole crossed the central meridian with respect to Earth some 9 days prior to the Solar Orbiter campaign on 2023 April 17. To this end, we supplemented Solar Orbiter data with photospheric magnetic field and coronal images obtained by the Solar Dynamics Observatory (SDO) (Pesnell et al. 2012), by selecting appropriate instances when the coronal holes were visible in the Earth line-of-sight. To gain context to the underlying surface magnetic field distribution of the coronal holes we employed photospheric line-of-sight magnetic field maps recorded by the Helioseismic and Magnetic Imager (HMI) (Scherrer et al. 2012) onboard the SDO. These data have an image scale of about  $0.5'' \text{ pixel}^{-1}$ . For coronal context, we used the EUV data from the Atmospheric Imaging Assembly (Lemen et al. 2012) onboard the SDO. In particular, we used EUV images from the  $171 \text{ \AA}$  (Fe ix: 5.85),  $193 \text{ \AA}$  (Fe xii: 6.2),  $211 \text{ \AA}$  (Fe xiv: 6.3) filters. Details in parentheses include ion species with dominant contribution to the EUV emission along with the logarithm of the peak formation temperature of those ions in the respective filters (Boerner et al. 2012). These level-1 AIA EUV data have an image scale of  $0.6'' \text{ pixel}^{-1}$ .

We deconvolved the AIA EUV data with the point spread functions (PSF) of the respective channels using AIAPY Python package (Barnes et al. 2020, 2021). This step reduces the artifacts in the data caused by filter mesh and PSF diffraction patterns. The deconvolved SDO AIA and HMI data are all processed using the `aia_prep` procedure in the `solarsoft` library (Freeland & Handy 1998). The resulting processed data have an image scale of  $0.6'' \text{ pixel}^{-1}$  and solar north is oriented up. The context AIA and HMI images from the two datasets along with the time-stamps are displayed in panels C and D of Figs. A.4 and A.6, respectively. Long-term changes in the spatial distribution of the magnetic field underlying coronal holes from the two observing periods are compared using SO/PHI-HRT and the SDO/HMI magnetograms in the FOV covered by the  $\text{HRI}_{\text{EUV}}$  data (Figs. A.5 and A.7). In the case of the April 2023 observations, the coronal hole section remains dominated by positive polarity magnetic fields, but in the case of the 2022 October observations, a magnetic bipole emerged in the coronal hole section that was previously observed by the Solar Orbiter.

### A.4. GOES data

In order to visualize the off-limb structure of the coronal holes under investigation, we made use of the  $171 \text{ \AA}$  EUV filter data acquired by the Solar Ultraviolet Imager (SUVI) (Darnel et al. 2022) on board the Geostationary Operational Environmental Satellites. The coronal hole from the first observing campaign

was near the west limb from the vantage point of SUVI around 2022 October 16. The second coronal hole was near the east limb from the perspective of SUVI around 2023 April 16. We used SUVI Level-1B data from these dates to investigate the off-limb structures of the coronal hole. The exact time stamps of the data that we used are added in panels B and D of Fig. D.1.

Locations of coronal holes from the EUV images were identified in the other datasets using the Carrington coordinate system and World Coordinate System information available in the metadata of those observations (Thompson 2006).

In Fig. D.2 we zoom into the respective quadrants of the SUVI images where the coronal hole off-limb structures appear. To enhance the off-limb features, we applied a radial filter (Seaton et al. 2023) to the SUVI images and then applied a multi-scale Gaussian normalization technique (Morgan & Druckmüller 2014).

### A.5. Space-time maps to analyze jet dynamics

To retrieve propagating signatures of the faint picoflare jets, we have constructed space-time maps along the length of each jet. The jet locations are marked by slits (S1–S7 in Fig. 2 and S1–S8 in Fig. 4). These slits have widths of 11 pixels (corresponding to about  $1.2 \text{ Mm}$ ) and their lengths typically cover the visible portion of each jet before it fades away in the background. To construct the space-time maps, we first average the intensity over the width from the jitter-removed level-2  $\text{HRI}_{\text{EUV}}$  data and stack the resulting intensity along the length of the slit as a function of time. Such maps reveal slanted intensity ridges due to the jet propagation. We smooth-subtract the space-time maps to enhance the contrast of the propagating features. The contrast-enhanced slanted ridges are shown in Fig. 2B–H and Fig. 4B–I.

The speed of the jet is then determined by the slope of the ridge in the space-time map. To measure the slope, we first identify the temporal position of the ridge along its length in the space-time map. To locate the temporal position of the ridge, we fit a Gaussian model to the time series of average intensity at each position along the slit. We used the `MPFIT` code (Markwardt 2009) for the Gaussian fitting. Peak, centroid and standard deviation of the Gaussian, plus constant and linear terms are the five fitting parameters that we considered. Determination of the temporal position is limited by the uncertainties in the intensity. To retrieve the associated  $1\sigma$  uncertainty in the determined temporal position, we supplied the code with the intensity uncertainties as input for error analysis. Given the exposure-normalized intensity  $I$ , exposure time  $t$ , sample size  $n$ , photons to digital number (DN) conversion factor,  $\alpha = 7.29 \text{ DN photon}^{-1}$  and readout noise  $r = 2 \text{ DN}$  for the  $\text{HRI}_{\text{EUV}}$  instrument (Gissot et al. 2023), intensity uncertainty is given by

$$\sigma = \sqrt{r^2 + \frac{It\alpha}{n}}. \quad (\text{A.2})$$

The temporal positions along the length of the slit are then fitted with a linear function to determine the jet speed. The  $1\sigma$  uncertainties in the temporal position are propagated to estimate the errors associated with the measured jet speed.

We studied the intensity fluctuations transverse to the jet length by placing the slits perpendicular to the jets as shown in Fig. 6A. We found that the transverse motions are better seen in the difference images. To demonstrate these motions we used the higher cadence  $\text{HRI}_{\text{EUV}}$  data of the coronal hole from 2022 October 13. To create a sequence of the difference images, we subtracted the first image from the sixth image, second image

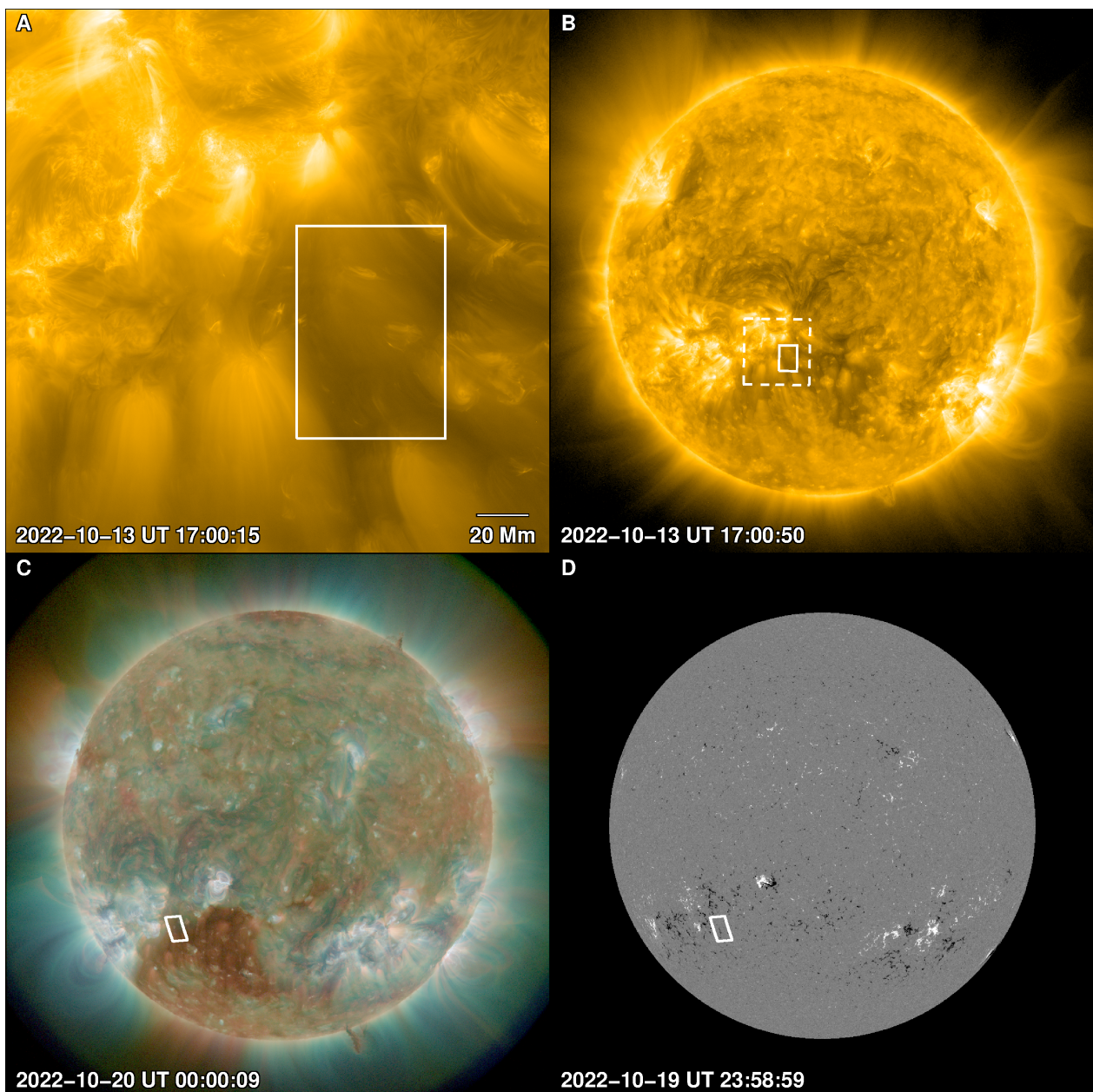


**Fig. A.4.** Overview of the coronal hole from the 2022 October observing campaign. (A) Full FOV of the  $\text{HRI}_{\text{EUV}}$  data showing the coronal hole in the lower half of the image. The boxed region outlines the dark portion within the coronal hole. The FOV of this region is marked as a solid rectangle in panels E and F of Fig. 1. A processed version of this view is displayed in Fig. 2A. (B) FSI image overlaid with the full FOV of panel A as dashed box. The dark portion of the coronal hole from panel A is outlined by a solid rectangle. (C) A composite image based on the SDO/AIA EUV images (red: 171 Å; green: 193 Å; blue: 211 Å). (D) SDO/HMI line-of-sight magnetogram, saturated at  $\pm 200$  G (positive polarity represented by lighter shaded regions while the negative polarity is represented by darker shaded regions). In both these panels the solid rectangle is the region covered by the solid rectangle from panel A.

from the seventh image and so on. These difference images are then used to create the space-time maps, which were then further processed by a  $3 \times 3$  pixel smoothing to improve the signal of the coherent features. These smoothed space-times maps for a sample of four jets are displayed in Fig. 6B–E. Movie S3 shows one example of these transverse motions. The movie is created by smoothing the difference images by a kernel of size  $3 \times 3 \times 3$  units, where the first two numbers correspond to pixels in the spatial ( $x, y$ ) directions, and the last number corresponds to the timesteps.

#### A.6. Jet speeds

In Figs. 2 and 4 we found that the picoflare jets have speeds in the range of  $\sim 100 \text{ km s}^{-1}$  and there are hints of repetitive jet activity. Such speeds appear to be common in a variety of coronal jets, irrespective of their surrounding regions. High-resolution observations have revealed that small-scale coronal jets launched in open-field coronal holes or closed-field active regions or the quiet-Sun corona exhibit repetitive signatures with speeds in the range of  $\sim 100 \text{ km s}^{-1}$  (Chitta et al. 2021; Mandal et al. 2022; Cheng et al. 2023). Repetitiveness or quasi-periodicity is also

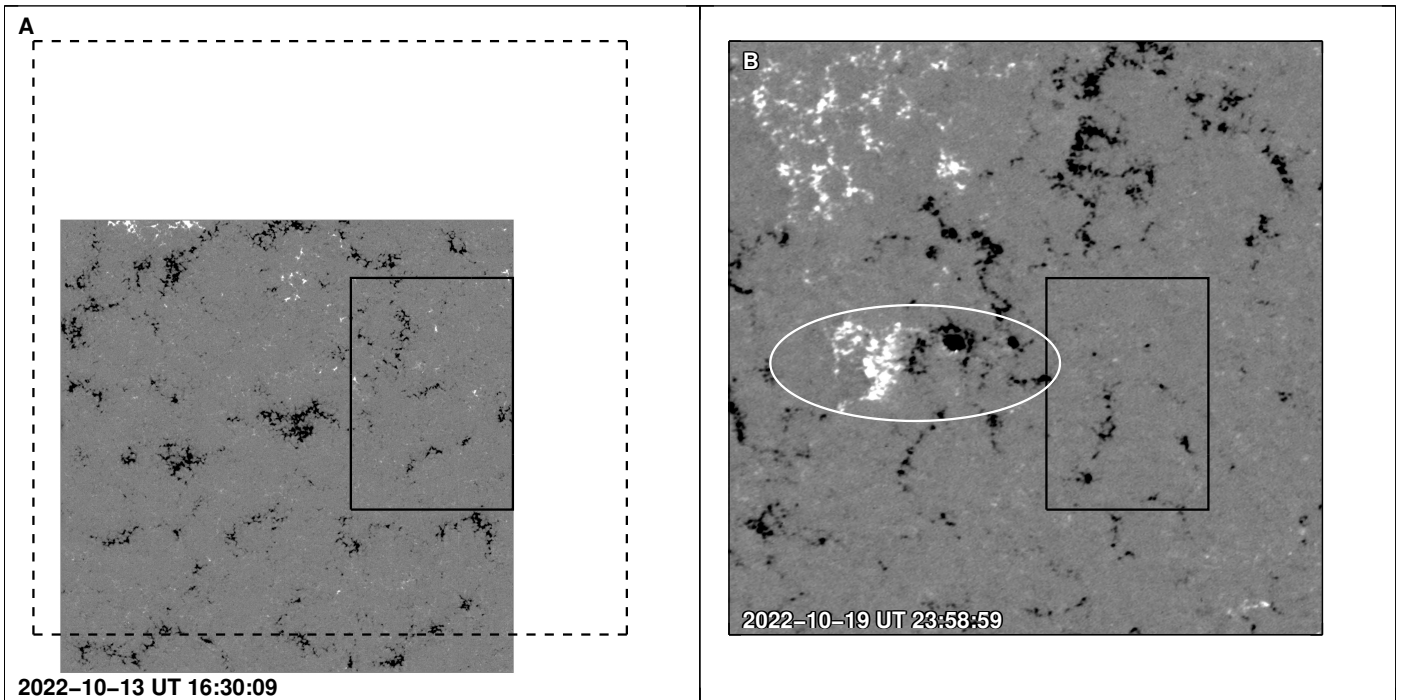


**Fig. A.5.** Surface magnetic field distribution. (A) SO/PHI-HRT magnetogram recorded 30 minutes prior to the start of the HRI<sub>EUV</sub> observations on 2022 October 13. The FOV is dominated by the negative polarity magnetic field of the coronal hole. The dashed rectangle outlines the full FOV of the HRI<sub>EUV</sub> images. The solid rectangle covers the coronal hole region that we analyzed. (B) The SDO/HMI magnetogram covering the same Carrington coordinates as the full FOV of HRI<sub>EUV</sub> images (i.e., the dashed rectangle in panel A), but some 6 days later. The solid rectangle covers the position of the coronal hole section that we analyzed on the HMI map. In both maps the magnetic field strength is saturated at  $\pm 200$  G. The white ellipse in panel B encloses a newly emerged magnetic bipole in the FOV after the 2022 October 13 Solar Orbiter campaign. This bipole can also be seen in the synoptic radial magnetic field map (adjacent to the solid white rectangle in Fig. 1E), which caused the appearance of brighter loop-like emission patterns near the northern section of the coronal hole as seen in the synoptic coronal map (Fig. 1F).

observed in the case of jets associated with bright ray-like plume structures in coronal holes (Kumar et al. 2022).

Jets propagate along the open magnetic field, but their speeds are measured in the plane-of-sky. In the case of the fast wind streams (Fig. D.1A), magnetic field lines near the northern section of the region considered for the expansion factor calculation (i.e., the region that is latitudinally closer to the observed picoflare jets), make angles of about  $55\text{--}60^\circ$  with respect to the plane-of-sky. Thus, the speeds of jets along the magnetic field lines will be above  $\sim 150 \text{ km s}^{-1}$ , which is over the sound speed of  $\sim 85 \text{ km s}^{-1}$  to  $\sim 100 \text{ km s}^{-1}$  in coronal holes and therefore, the jets we observed are not related to slow magnetoacoustic waves (Chitta et al. 2023b).

## Appendix B: Solar wind Alfvénicity

A measure of the Alfvénicity ( $C_{VB}$ ) of the solar wind is defined as the covariance of the solar wind parameters, velocity  $V$  and magnetic field  $B$ , normalized by the product of their standard deviations (D’Amicis et al. 2021a), which is given by

$$C_{VB} = \frac{\sum_j (V_j - \bar{V})(B_j - \bar{B})}{\sqrt{\sum_j (V_j - \bar{V})^2 (B_j - \bar{B})^2}}, \quad (\text{B.1})$$

where  $j$  denotes the index of the time series of a given variable. For the purpose of this calculation, we used only the N component as it is more Alfvénic than the other two (Tu et al. 1989).  $B_N$  was averaged at the plasma sampling time and expressed in

Alfvén units (normalized to  $\sqrt{4\pi\rho}$ , where  $\rho$  is the mass density).  $\bar{V}$  and  $\bar{B}$  are averages of the velocity and magnetic field over 30 minute intervals. The plotted  $C_{VB}$  in Figs. 1 and 3 is then derived from a 30 minute running average. This time scale is a typical Alfvénic scale at those heliocentric distances as shown by the Helios spacecraft (Tu et al. 1989).

## Appendix C: Magnetic connectivity: Tracing footpoints of the solar wind magnetic field

To investigate the global magnetic topology we considered Carrington (synoptic) maps as the lower boundary condition to extrapolate coronal magnetic fields based on a potential field source surface (PFSS) technique (Schatten et al. 1969; Schrijver & De Rosa 2003). The first of the Solar Orbiter observing campaigns was during the Carrington rotation number (CR) 2263, while the second observing campaign period was covered by CR2269. In particular, we used SDO/HMI synoptic maps of type `hmi_synoptic_mr_polfil_720s`, in which the magnetic field at higher latitudes ( $> 60^\circ$ ) of a given pole is inferred from the annual observations of that pole when it is most visible from Earth (Sun et al. 2011). Magnetic field extrapolations were performed using a PFSS code available in SolarSoft. The source surface or the top boundary is placed at a nominal height of 2.5 solar radii ( $R_\odot$ ), from the center of the Sun. Above this source surface, the magnetic field is assumed to remain radially open. The extrapolations were carried out on a mesh size of  $(r, \phi, \vartheta) = (172, 720, 360)$ , in the radial ( $r$ ), longitudinal ( $\phi$ ), and latitudinal ( $\vartheta$ ) directions. This mesh size corresponds to a

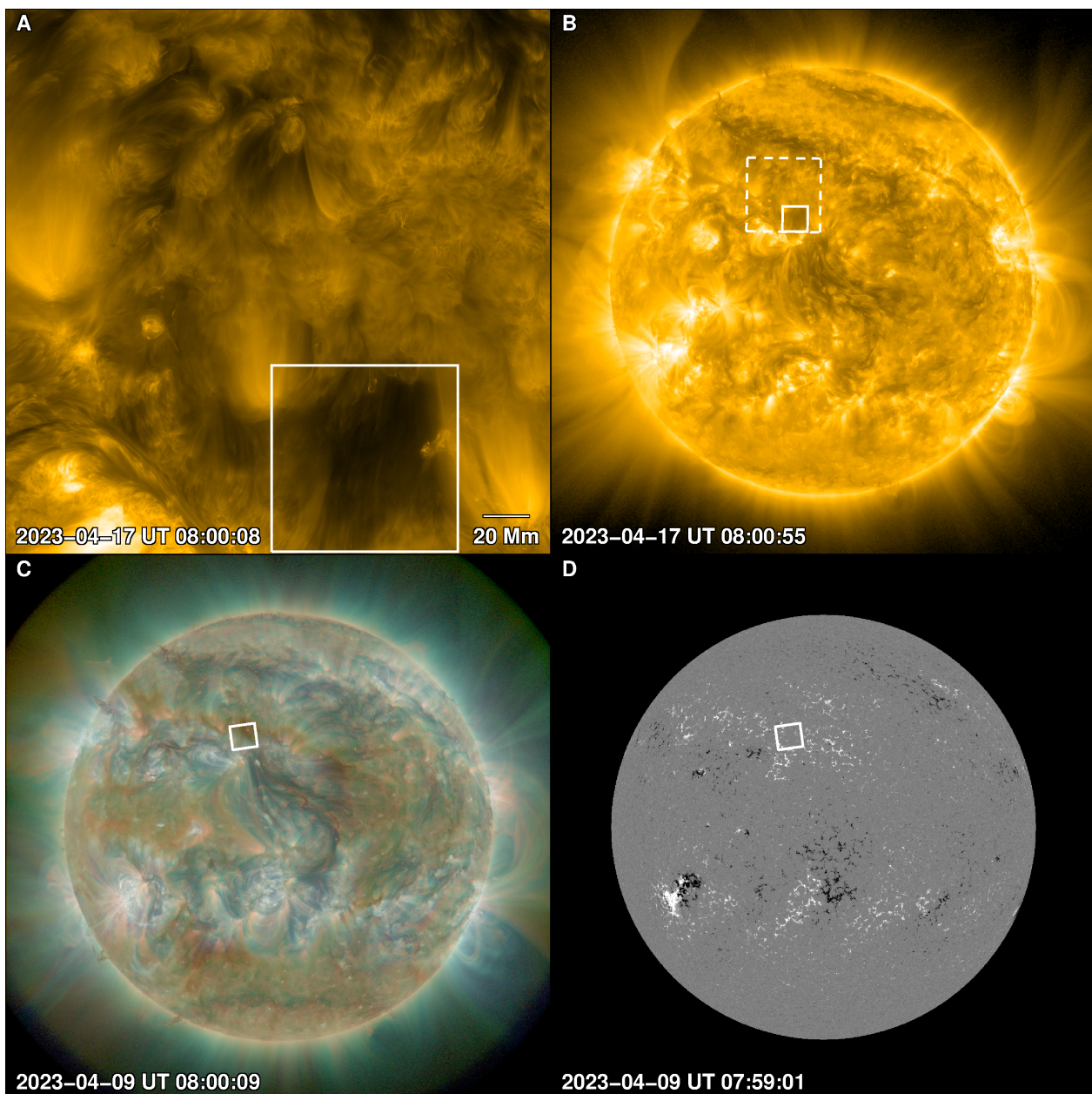


**Fig. A.6.** Overview of the coronal hole from the 2023 April observing campaign. Same as Fig. A.4 but plotted for the coronal hole observed on 2023 April 17. In this case, the SDO images were taken 8 days prior to the Solar Orbiter campaign.

grid spacing of  $0.5^\circ$  in the longitudinal, and latitudinal directions, and  $8.77 \times 10^{-3} R_\odot$  in the radial direction.

Then we traced the footpoints of the interplanetary magnetic field to the solar surface by employing the two-step ballistic back-mapping technique that first identifies the magnetic connectivity of the solar wind plasma to the source surface using the in-situ radial velocity measurements (assuming no acceleration), and then connects the field lines from the source surface to the solar surface using the PFSS extrapolations (Nolte & Roelof 1973). The in-situ solar wind radial velocity measurements, averaged over 1 hour, were used for this purpose. We used the solar rotation profile  $\omega(\vartheta)$  as a function of heliographic latitude ( $\vartheta$ ), given by  $\omega(\vartheta) = 14.50 - 2.87 \sin^2 \vartheta$  degree  $\text{d}^{-1}$  (Poljančić Beljan et al. 2017) to estimate the solar rotation during the travel time of the wind parcel from the source surface to the spacecraft. We then traced the magnetic field lines from the source surface at

$2.5R_\odot$  back to the solar surface using the PFSS model. Uncertainties in the longitudinal connectivity at the source surface based on the ballistic back-mapping technique are  $\sim 10 - 16^\circ$ , at least for the case of the slow wind streams detected near Earth, and are somewhat lower for the fast wind streams (Nolte & Roelof 1973; Macneil et al. 2022; Koukras et al. 2022).

Assuming radial propagation of the solar wind with constant speed from the source surface, the solar wind plasma parcel observed in-situ around 11 UT on 2022 October 14 would have left the Sun some 18 hours earlier, the period that is close to the start time of the Solar Orbiter remote-sensing campaign on 2022 October 13. Similarly, the solar wind parcel recorded around 08 UT on 2023 April 19 would have left the Sun 48 hours earlier, the period that is close to the start time of the Solar Orbiter remote-sensing campaign on 2023 April 17 at 08:00 UT.

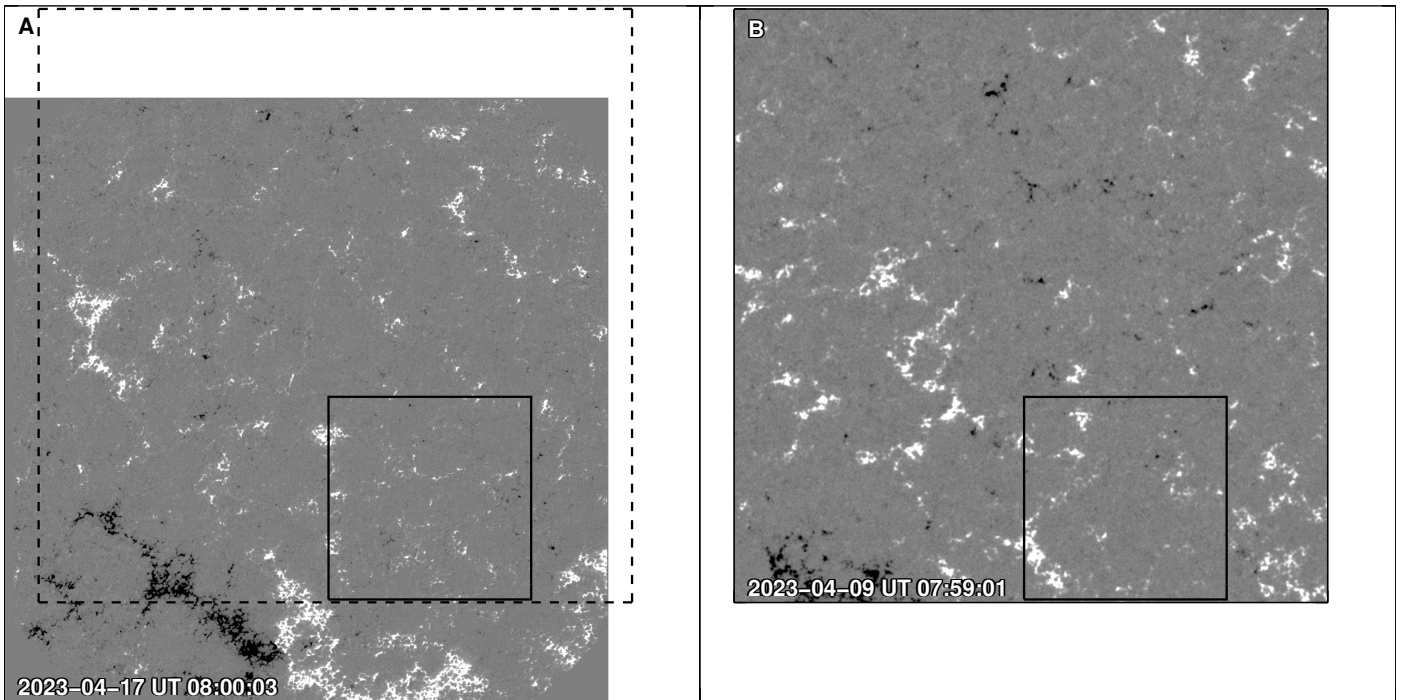


**Fig. A.7.** Surface magnetic field distribution. Same as Fig. A.5 but plotted for the coronal hole observed on 2023 April 17. Here the dominant polarity of the magnetic field is positive.

This two-step ballistic back-mapping approach to trace the source region of the solar wind is rather simplistic. A more realistic approach needs to consider the effects of acceleration of solar wind and corotation. However, to estimate the effects of corotation, i.e., to compute the tangential flow, information on the profiles of Alfvén speed and radial density are required. Deviations in the source region longitudes, as well as the latency in the travel times of a solar wind parcel, between these two approaches have been compared recently (Dakeyo et al. 2024). It is shown that between the two approaches, for the range of Solar Orbiter distances applicable in this study (i.e., 63 to 71  $R_{\odot}$ ) near the ecliptic plane, deviation in the source region longitudes is at most  $1^{\circ}$  in the case of the fast wind with speed  $>550 \text{ km s}^{-1}$ , and at most  $4^{\circ}$  in the case of the slow wind with speed  $<350 \text{ km s}^{-1}$ . Latency in the travel times could be about 2 h in the case of the fast wind, and in the range of 15 to 30 h in the case of the slow wind (Dakeyo et al. 2024).

As shown in Figures 1 and 3, magnetic connectivity points assuming ballistic back-mapping technique are all clustered within  $5^{\circ}$  to each other. Therefore, with respect to the given bottom boundary condition, i.e., synoptic map of the radial component of the magnetic field, longitudinal connectivity uncertainties caused by not using a more realistic tracing of the solar wind plasma are less than the spread of the points themselves. For the fast wind, travel time uncertainty between the two methods is less than the duration of the 24 h interval that we considered to back-map the solar wind source region. In the case of the slow wind, travel time uncertainty is comparable or larger than the 24 h interval. This becomes important when the underlying source region evolves rapidly than this timescale. But as we show in Fig A.6, the small coronal hole persists for several days and the underlying magnetic field distribution has not changed considerably. This implies that despite longitudinal connectivity and or travel time uncertainties, the spacecraft might be connected to

the same source regions that were exhibiting prevalent picoflare jet activity in both cases of coronal holes.

#### Appendix D: Coronal hole flux-tube expansion

The expansion factor  $f_{ss}$  measures the rate of expansion of a flux tube between the photosphere and the source surface (Hundhausen 1972; Wang & Sheeley 1990), and is defined as

$$f_{ss} = \left( \frac{R_{\odot}}{R_{ss}} \right)^2 \frac{B_p(R_{\odot})}{B_p(R_{ss})}, \quad (\text{D.1})$$

where  $R_{\odot}$  is the solar radius representing the height of the photosphere from the center for the Sun,  $R_{ss} = 2.5R_{\odot}$ , is the height of the source surface.  $B_p(R_{\odot})$  and  $B_p(R_{ss})$  are the magnetic field strengths at the photosphere and the source surface.

The flux-tube expansion factor is calculated for magnetic field lines associated with the coronal holes. In the case of the 2023 April coronal hole, we took a  $10^{\circ} \times 10^{\circ}$  region on the Carrington map covering the analyzed coronal hole section (Fig. 3). But in the case of the 2022 October coronal hole, a magnetic bipole emerged close to the dark section of the coronal hole we considered a few days after the Solar Orbiter campaign (region outlined by an ellipse in Fig. A.5), which was then registered in the Carrington map CR2263. This is also the reason why the coronal section of the Carrington map (Fig. 1F) shows brighter loop-like emission patterns near the region that was earlier occupied by the darker sections of the coronal hole as captured by the EUV data Fig. A.4. As the bipole would locally change the magnetic topology, which in turn affects the expansion factor computation, we considered a representative darker coronal hole section situated at a longitudinal separation  $\sim 15^{\circ}$  from the original region for the determination of  $f_{ss}$  (Fig. 1). For both cases then, the expansion factor, which is a dimensionless parameter, is calculated for a set of about 4000 magnetic field lines open

to the source surface that are connected to the selected region on the photosphere. In Fig. 5 we plot the distribution of the flux-tube expansion factor of coronal holes measured at the source surface for the fast and Alfvénic slow wind cases. The histograms have a bin size of 2 units and are normalized to their peak value.

We visualized the coronal hole expansion using the GOES/SUVI EUV images. The field lines traced from the above step are compared with the coronal images for their topology. Overall, the observed off-limb features surrounding the considered coronal hole sections match well with the field lines traced in the PFSS extrapolations. In particular, the observed features corresponding to the larger coronal hole generating the fast wind in October 2022 were more streamlined while those related to the slow wind case from April 2023 show rapid expansion (Figs. D.1 and D.2). These similarities between the observations and extrapolated field lines add credence to our magnetic modeling based on the PFSS technique.

### Appendix E: Captions for Movies S1 to S3

**Movie S1:** Animated version of Fig. 2A, showing widespread picoflare jet activity in the larger coronal hole from 2022 October, linked to the fast wind streams.

**Movie S2:** Animated version of Fig. 4A, showing widespread picoflare jet activity in the smaller coronal hole from 2023 April, linked to the Alfvénic slow wind streams.

**Movie S3:** Animation showing the Alfvénic pulse launched by the picoflare jet tagged with slit S0 in Fig. 6B. The field of view is  $9.5 \text{ Mm} \times 9.5 \text{ Mm}$ , covering a duration of 8.3 min.

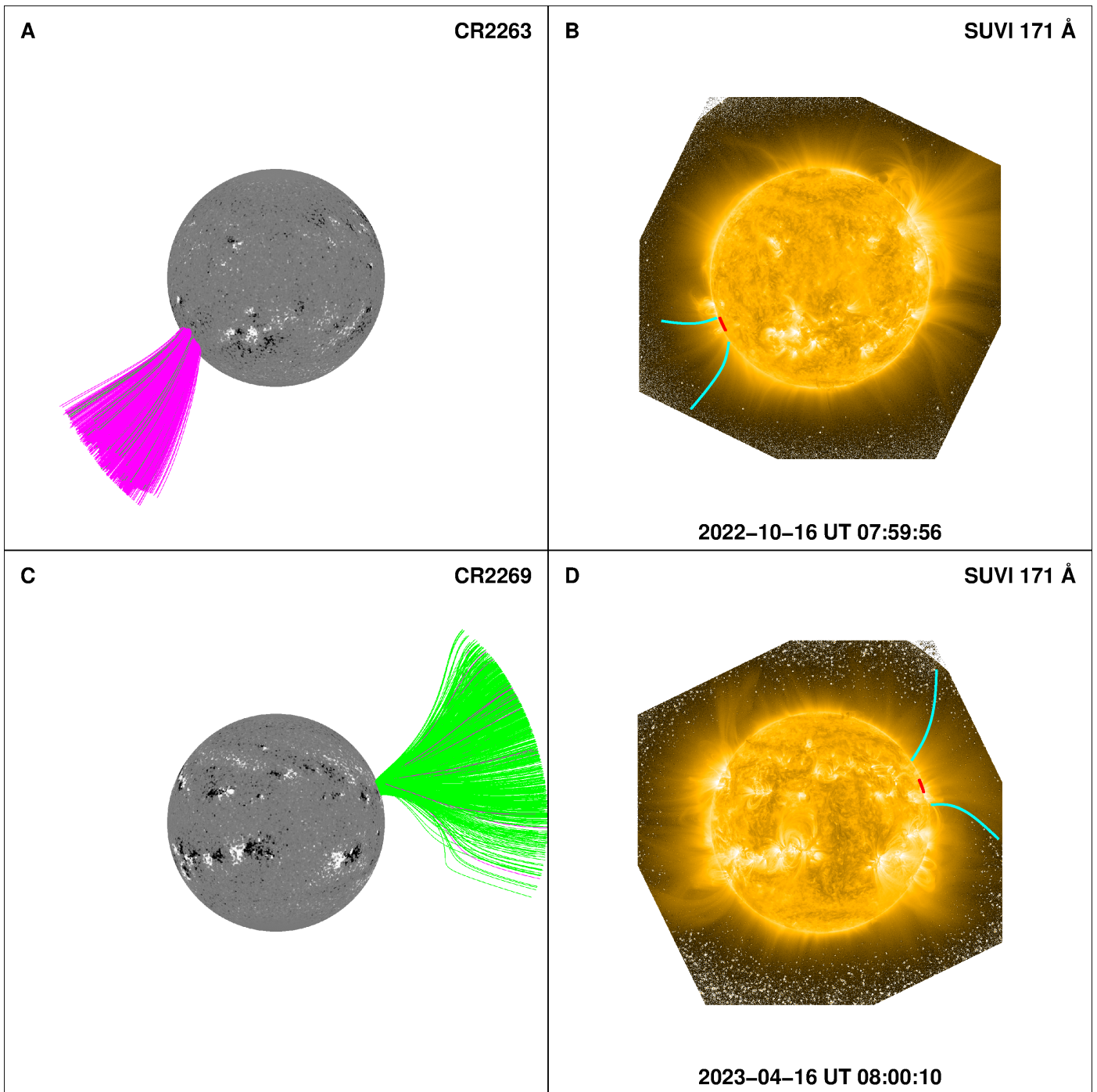


**Fig. D.1.** Visualizing the expansion of coronal holes. (A) CR2263 synoptic map rendered as a sphere, with FOV of  $5 R_{\odot} \times 5 R_{\odot}$ . Radial magnetic field strength saturated at  $\pm 100$  G. The lines trace magnetic field lines from the coronal hole location at the solar surface to the source surface at  $2.5 R_{\odot}$ . (B) GOES/SUVI 171 Å passband image showing the section of the October 2022 coronal hole projected at the east limb (marked by the red line). The cyan colored lines outline the coronal hole structure on the plane-of-sky. (C) Same as panel A but plotted for the case of CR2269. (D) Same as panel B but plotted for the case of the April 2023 coronal hole. Zoomed-in views of the observed coronal hole sections are further displayed in Fig. D.2.

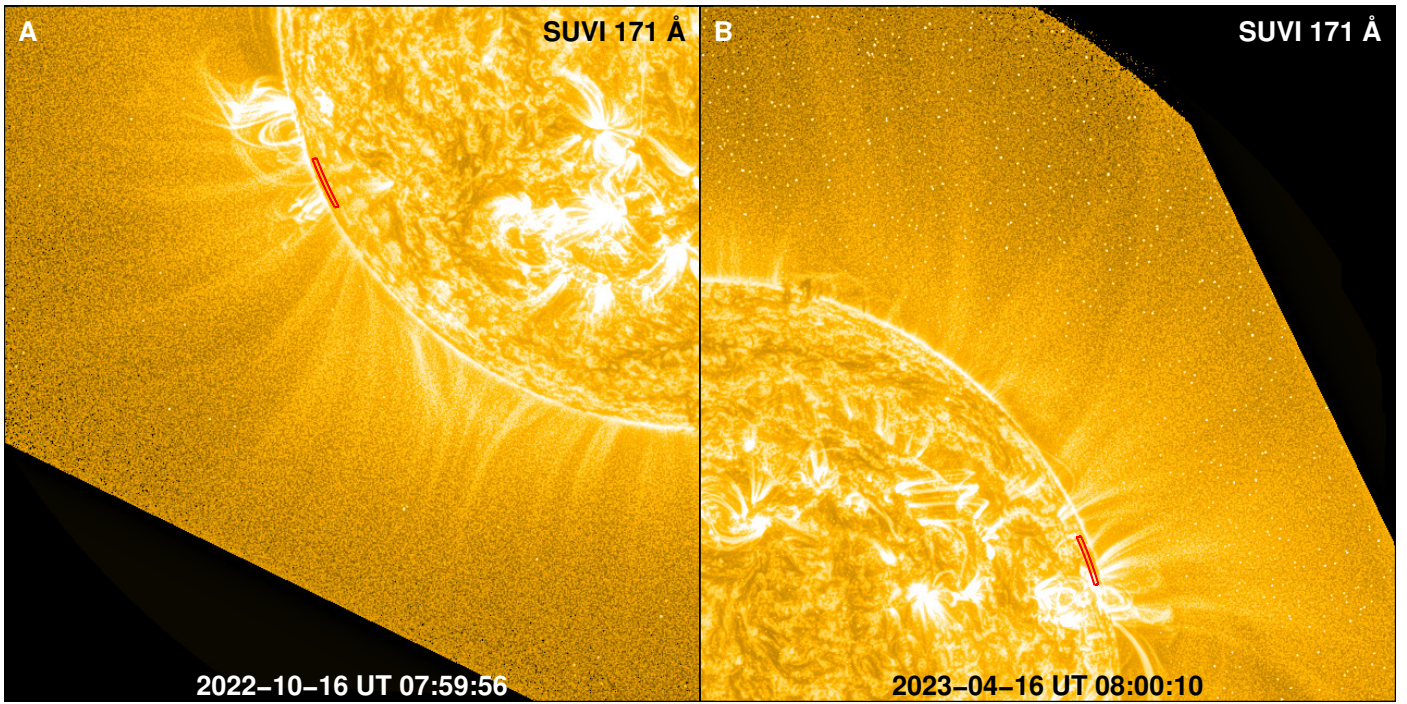


**Fig. D.2.** Visualizing the expansion of coronal holes. (A) Zoom into the south-east quadrant of the SUVI image shown in Fig. D.1B, but without the cyan colored lines overlaid. The section of the October 2022 coronal hole projected at the east limb is marked by the red line. (B) Zoom into the north-west quadrant of the SUVI image displayed in Fig. D.1D, for the case of April 2023 coronal hole.